Title

Seismic Performance of Underground Reservoir Structures: Insight from Centrifuge Modeling on the Influence of Structure Stiffness

Journal

Journal of Geotechnical and Geoenvironmental Engineering, 142(7)

ISSN

1090-0241

Authors

Hushmand, A
Dashti, S
Davis, C
et al.

Publication Date

2016-07-01

DOI

10.1061/(asce)gt.1943-5606.0001477

Peer reviewed

Seismic Performance of Underground Reservoir Structures: Insight from Centrifuge Modeling on the Influence of Structure Stiffness

A. Hushmand[1], S. Dashti[2], C. Davis[3], B. Hushmand[4], M. Zhang[5], M. Ghayoomi[6], J.S. McCartney[7], Y. Lee[8], J. Hu[9]

ABSTRACT: The available simplified analytical methods for the seismic design of underground structures either assume *yielding* or *rigid-unyielding* conditions. Underground reservoir structures do not fall into either of these categories. In this paper, we present the results of three centrifuge experiments that investigate the seismic response of *stiff-unyielding* buried structures in medium dense, dry sand and the influence of structure stiffness and earthquake motion properties on their performance. The structure to far-field spectral ratios were observed to amplify with increased structural flexibility and decreased soil confining pressure at the predominant frequency of the base motion. Lateral earth pressures and racking displacements for a range of structural stiffnesses were compared with procedures commonly used in design. Pre-earthquake measured lateral earth pressures compared well with expected at-rest pressures. However, none of the commonly used procedures adequately captured the structural loading and deformations across the range of stiffness and ground motions for which these reservoirs must be designed. Further, it is unclear if the current methods of analysis provide conservative or unconservative results for engineering design purposes. This identifies a critical need for improved methodologies to analyze and design underground reservoir structures.

[1] Graduate Student Researcher, University of Colorado Boulder, Civil, Env. and Arch. Engineering, Boulder, CO.
[2] Assistant Professor, Univ. of Col. Boulder, Civil, Env. and Arch. Eng., Boulder, CO, shideh.dashti@colorado.edu.
[3] Trunk Line Design Manager, Los Angeles Department of Water and Power, Los Angeles, CA.
[4] President and Principal Engineer, Hushmand Associates, Inc., Irvine, CA.
[5] Centrifuge Engineer, Civil Eng., Univ. of Colorado Boulder, Boulder, CO.
[6] Assistant Professor, University of New Hampshire, Durham, NH.
[7] Associate Professor, University of California at San Diego, San Diego, CA.
[8] Civil Engineering Associate, Los Angeles Department of Water and Power, Los Angeles, CA.
[9] Civil Engineering Associate, Los Angeles Department of Water and Power, Los Angeles, CA

INTRODUCTION

The current methods used to analyze the seismic response of underground box structures are based on simplified analytical or numerical tools that have not been adequately validated against full scale field measurements or physical model studies. Furthermore, the kinematic constraints of these structures are not fully captured by simplified seismic design procedures. Soil-structure-interaction (SSI) for these buried structures is complex and depends on foundation fixity, properties of the surrounding soil, flexibility of the structure relative to soil, and the characteristics of the earthquake motion. There is an increasing need in engineering practice to obtain a better understanding of the seismic performance of these underground structures. For example, the Los Angeles Department of Water and Power (LADWP) is replacing some of its open water reservoirs with buried, reinforced-concrete reservoirs to meet water quality regulations. Understanding the seismic performance of these restrained underground structures will improve the structural and geotechnical seismic design of these type of projects.

Traditionally, underground structures are categorized either as *yielding* or *rigid-unyielding*, and are designed differently based on the categorization. A *yielding* wall is one that displaces sufficiently to develop an active earth pressure state. The current state of practice for assessing seismic earth pressures on *yielding* structures relies heavily on the Mononobe-Okabe (Okabe 1926; Mononobe and Matsua 1929) and Seed-Whitman (Seed and Whitman 1970) methods. For *rigid-unyielding* walls that don't undergo any deformation, the method of choice is often the simplified solution proposed by Wood (1973), which assumes a completely rigid wall (with no flexure). Underground reservoir structures fall in between the two extreme cases of *yielding* and *rigid-unyielding*, because they are not completely rigid, as they exhibit some deformation. But their deformation is less than that of a vertical element in the ground because of the restraint provided by the floor and roof of the structure. Therefore, in this paper, these buried reservoir structures are classified as *stiff-unyielding* structures.

The primary factors in the seismic design of underground box structures include: 1) seismic lateral earth pressures; 2) magnitude and location of lateral thrust; 3) bending strain and moment distribution; and 4) racking deformations. Although recent physical model studies have evaluated the seismic performance of *yielding* retaining walls (e.g., Al Atik 2010 and Mikola 2012), the seismic response of *stiff-unyielding* underground structures has not been sufficiently evaluated experimentally in order to validate the numerical tools used in design.

A series of fourteen centrifuge experiments were conducted at the University of Colorado Boulder to evaluate the seismic performance of relatively stiff underground structures buried in granular soils. The structure stiffness, backfill soil type and slope, embedment, container type (rigid versus flexible boundaries), fixity conditions, and ground motion characteristics were varied to evaluate their influence and relative importance on structural performance. Three different model box structures were designed to represent simplified prototype reinforced concrete buried reservoirs of varying stiffness characterizing those evaluated by the LADWP. The proposed reservoirs have 11 to 12 m high walls that will be buried and restrained against rotational movement at the top and bottom by the roof and floor, restricting deformation. Additionally, the reservoir's foundation can rock or slide laterally as it rests on soil. This paper focuses on a comparison of the behavior of the three structures having different stiffness values in tests with the same backfill soil, container, and base fixity. These experiments enabled a comprehensive and fundamental evaluation of the influence of structure stiffness and ground motion characteristics on seismic SSI for reservoir structures buried in medium-dense dry sand as well as lateral earth pressures, racking deformations, and bending strains and moments of these structures.

BACKGROUND

Underground box structures have historically performed well during earthquakes. However, a few cases of failure serve as reminders of the need to consider seismic loading in their design. Severe damage was sustained by the Daikai Subway Station during the 1995 Hyogo Ken Nanbu earthquake in Kobe, Japan. Many of the center columns of the box structure failed causing the roof to collapse and walls to crack. The station box structure was not designed for earthquake loading (Lew et al. 2010). Hradilek (1972) evaluated the damage to channel box culverts after the 1971 San Fernando earthquake. Most of the damage to these structures was attributed to permanent ground displacement or fault slippage, which caused large, permanent passive earth pressures. However, the underground structures were not designed for seismic loading at the time, and their damage could be partly caused by excessive seismic earth pressures. As an example, the walls of a reinforced concrete underground reservoir at the Balboa water treatment plant failed during the San Fernando earthquake (Wood 1973). The reservoir walls were 6.1 m high and restrained at the top and bottom, and the structure was buried in a soft fill deposit. With no evidence of soil liquefaction at the site, this failure may have occurred due to a combination of permanent ground movement and excessive seismic lateral earth pressures. The performance of building basements during previous earthquakes has generally been satisfactory, as reported by Lew et al. (2010).

Most analytical methods for evaluating dynamic earth pressures were inspired by the pioneering work of Mononobe-Okabe (Okabe 1926; Mononobe and Matsua 1929). The Mononobe-Okabe (M-O) method is based on Coulomb’s limit equilibrium earth pressure theory, with the addition of horizontal and vertical inertial forces due to seismic loading. They assumed total (static and dynamic) lateral earth pressures increase with depth in a triangular fashion, and the resultant force is applied at H/3 above the base, where H is the total height of the wall. A major assumption in this method is that the wall yields (or displaces) sufficiently to produce the minimum active pressure condition. Seed and Whitman (1970) later simplified the M-O method by separating the total lateral earth pressure coefficient, K_{ae}, into an active static lateral earth pressure coefficient, K_a, and a dynamic earth pressure coefficient increment, ΔK_{ae}. The Seed-Whitman (S-W) method uses an inverted triangle dynamic earth pressure profile with the resultant thrust applied at 0.6H above the base.

Wood's method (Wood 1973) was developed for infinitely rigid, restrained walls having a fixed base with a linear elastic soil backfill. For walls with very long backfills, the dynamic thrust from Wood's method is applied at 0.63H above the base of the wall (Ebeling and Morrison 1992). Equivalent static solutions were derived for the dynamic problems of interest. Variables not taken into account by the simplified Wood's method are: a soft, deformable foundation soil, an increase in soil modulus with depth, soil nonlinearity, and wave propagation with motion amplification (or de-amplification at large strains).

Veletsos and Younan (1994) numerically investigated rigid, yielding, and unyielding retaining walls with a linear viscoelastic soil backfill. They showed that increasing rotational flexibility at the wall base decreases dynamic earth pressures and the associated shear forces and bending moments acting on the wall. A few shortcomings of this method include: 1) assumption of complete bonding between the soil and a rigid base; 2) assumption of complete bonding between the wall and the soil; 3) no consideration for horizontal translation of the wall; and 4) the complexity of the solution and lack of simple computational steps for design applications.

Richards et al. (1999) proposed a simplified analytical method to determine the distribution of dynamic earth pressures on rigid, yielding, and unyielding retaining walls with a granular soil backfill, while taking into account soil's nonlinear and plastic behavior and wall's horizontal translation, but not wave propagation. Davis (2003) subsequently introduced a simplified analytical method to calculate dynamic earth pressures from propagating waves on the walls of a rigid-unyielding underground structure with a non-rigid base, taking into account the increase in small-strain shear modulus of the soil with depth but not soil nonlinearity.

Psarropoulos et al. (2005) performed finite element analyses on rigid and flexible walls to build upon the work of Veletsos and Younan (1994) by taking into consideration the influence of flexural wall rigidity, inhomogeneous backfill soil, and translational flexibility on the amplitude and distribution of earth pressures acting on the wall. Subsequently, Ostadan (2005) proposed a simplified method to calculate dynamic earth pressures acting on a rigid-unyielding basement wall with a rigid foundation, taking into account wave propagation and soil nonlinearity, but not the increase in shear modulus with depth. The resulting pressure envelopes proposed by Ostadan (2005) were similar to those of Wood (1973). Seismic earth pressures acting on deformable but stiff, unyielding underground box structures with realistic soil properties have not been adequately studied numerically. Further, many of the previous analytical and numerical methods were not sufficiently calibrated and validated against case histories or realistic physical model studies.

The majority of previous physical model studies have focused on the seismic response of *yielding* retaining walls under realistic pressures using the centrifuge (Ortiz 1982; Bolton and Steedman 1982; Steedman and Zeng 1991; Andersen 1991; Stadler 1996; Dewoolkar 1996; Nakamura 2006; Al Atik 2010; and Mikola 2012). Mikola (2012) studied the seismic response of a restrained basement wall in addition to a retaining wall. Both sets of experiments indicated that dynamic earth pressures increase with depth in a triangular manner and their magnitudes were generally less than those obtained from the M-O and S-W methods. This conclusion contradicted the method proposed by Ostadan (2005) for basement structures that were closer to Wood's method. Recent dynamic centrifuge tests have been performed on rectangular cross section tunnels in cohesionless soils by Cilinger and Madhabhushi (2011) and Tsinidis et al. (2015). However, these tunnels have much thinner linings and are buried much deeper than the structures evaluated in this study and are expected to have different behavior than *stiff-unyielding* structures near the surface. Some of the more complex conditions found in practice are often evaluated using numerical modeling techniques (e.g., Roth et al. 2010; Zhai et al. 2013), which have not been validated to conform to the seismic performance of *stiff-unyielding* structures.

In summary, the state of practice for the seismic design of underground box structures relies heavily on simplified analytical methods that either assume *yielding* or *rigid-unyielding* conditions. Analytical, numerical, and physical model studies have been limited on the class of *stiff-unyielding* underground box structures. Centrifuge modeling can help fundamentally evaluate soil-structure-interaction, deformations, and lateral earth pressures for this class of buried structures and the relative importance of different testing parameters on their seismic performance.

CENTRIFUGRE TESTING PROGRAM

Three centrifuge tests were performed with similar instrumentation and soil conditions but different model underground structures. The lateral stiffness and natural period was varied among the three model structures, which were buried in medium-dense, dry sand. The three experiments are referred to as T-Flexible, T-BL (baseline), and T-Stiff, based on the relative stiffness of the structures. Experiments were performed at 60g of centrifugal acceleration using the 400 g-ton centrifuge at the University of Colorado Boulder (Ko 1988). Earthquake motions were applied to the model specimen in flight using the servo-controlled electro-hydraulic shake table, which is mounted on the basket of the centrifuge. A series of five earthquake motions were applied to the base of the models in the same sequence in the three experiments.

Model Structure Design and Properties

The actual prototype reservoirs are complex structures with many columns and interior walls that support the weight of the roof slabs, walls resisting lateral shear forces, and other structural details, the 3D response of which is difficult to simulate properly in a scaled centrifuge model. Accordingly, simplified, equivalent prototype 2-D box structures were identified to match the mass, lateral stiffness, and natural frequency of the actual prototype reservoir structures. The dimensions of these equivalent prototype box structures were then converted to model scale dimensions at 60g, to design and fabricate three model structures referred to as Baseline (BL), Flexible, and Stiff (corresponding to experiments T-BL, T-Flexible, and T-Stiff, respectively). These model structures were designed with uniform 1018 Carbon Steel (density = 7870 kg/m^3; Young's Modulus = 200 GPa; Poisson's ratio = 0.29). The structural stiffness was varied by changing the thickness of the models and keeping all other dimensions (outer height, width, length) the same, as summarized in Table 1. The model structures were fabricated by welding steel plates to ensure a strong moment connection at the corners. The fundamental frequencies of the structures were estimated by performing 3-D finite element simulations of structures in Abaqus. These values were then confirmed experimentally using vibration tests on a shaking table at 1g, in which the structures were bolted to the shaking table using temporarily-welded steel tabs. The results are summarized in Table 1. The numerical and experimental values of fundamental frequency were consistent for all structures, confirming the validity of the model structures for simulating the prototype structures.

Preparation of Model Specimens

The instrumentation layout and testing configuration shown in Figure 1 was the same in all three tests. These tests were conducted using a transparent flexible shear beam (FSB) type container developed by Ghayoomi et al. (2012, 2013). Dry Nevada sand No. 120 (G_s=2.65; e_{min}=0.56; e_{max}=0.84; D_{50}=0.13 mm; C_u=1.67) was pluviated into the FSB container to achieve a uniform soil layer with a relative density of $D_r \approx 60\%$. This corresponds to a dry unit weight of 15.6 kN/m^3. The fundamental frequency of the far-field soil column at small strains ranged from approximately 2.1 to 2.4 Hz, while its effective fundamental frequency during different motions obtained from the transfer function of acceleration recordings at the surface to base ranged from approximately 1.0 to 1.7 Hz.

Model preparation began by placing accelerometers at the pre-selected locations during pluviation of the sand layer until the elevation of the structure base was reached (Figure 1). Teflon sheets were placed between the sidewalls of the container and on the ends of the structure to allow relative sliding and minimize friction, in order to simulate plane strain conditions. The structure was placed in the middle (along the length) of the FSB container followed by sand pluviation on the two sides of the structure until reaching its top elevation. A photograph taken of the completed model from the side of container is shown in Figure 2.

Instrumentation

As shown in Figure 1, data was acquired from accelerometers (A1-A16), LVDTs (D1-D7), tactile pressure sensors (TP1-4), and strain gauges (SG1-16). Accelerometers were placed horizontally at the container base, on the structure, and within the soil at different elevations to monitor movement. The accelerometer array A1-4 representing far-field conditions (approximating free-field) was placed 11.1 m from the structure wall toward the flexible container boundary (3.7 m from container boundary).

LVDTs were used to measure the settlement of soil and structure as well as the lateral displacement of structure and the FSB container top frame. Eight strain gauges were installed on each wall of the structure to measure bending strains and hence, bending moments. Tactile pressure sensors are flexible, thin sheets containing a matrix of sensors, which may be used to measure total earth pressures. Four high speed, tactile pressure sensors (model 9500) manufactured by Tekscan Inc. were used to measure total pressures on both sides of the structure. Each tactile sensor has a total of 196 sensels in 14×14 grid with a spacing of 5.1 mm in model scale. Each of the 196 sensels recorded pressure simultaneously at a rate of 4,000 samples per sec (sps) during dynamic loading. All other instruments on the National Instruments data acquisition system recorded data at 3,000 sps during shaking.

Tactile sensors were known to underestimate the full amplitude content of a dynamic signal in the high frequency environment of the centrifuge (Olson et al. 2011). This is partially caused because older sensor models under-sampled the dynamic signals. It is recommended to sample at least 10 times as fast as the highest frequency in the signal to ensure that it is accurately reconstructed in the time domain (Derrick 2004). Centrifuge shake tables typically cannot produce controlled motions at frequencies greater than approximately 300 Hz (model scale). Hence, a minimum sampling rate of about 3,000 sps is required in dynamic centrifuge experiments, which was satisfied in these tests.

The inability to measure the full amplitude of the dynamic pressure signal is also partially caused by the tactile sensor's frequency-dependent response, which needs to be characterized and accounted for (Dashti et al. 2012). By characterizing how the sensor records load over a range of frequencies, a transfer function was developed and applied to sensor recordings to compensate for the loss of pressure amplitude. This frequency-dependent, amplitude correction procedure is referred to as the sensor's dynamic calibration (detailed by Gillis et al. 2015).

The tactile sensors were first thoroughly de-aired by creating small holes to allow air to vent followed by sealing, according to the procedure recommended by Tessari et al. (2014). After they were conditioned and equilibrated, these sensors were statically calibrated using a pneumatic loading device and a fine sandpaper, as recommended by Tessari et al. (2014). Then, they were dynamically calibrated using the procedure described by Gillis et al. (2015).

Ground Motions

A suite of base motions were first selected by LADWP for the specific site of interest, here referred to as *desired* motions. These motions included scaled versions of the horizontal acceleration recordings at the Sylmar Converter Station during the 1994 Northridge Earthquake (NSC52), the LGPC Station during the 1989 Loma Prieta Earthquake (LGP000), and the Istanbul Station during the 1999 Izmit Earthquake in Turkey (IST180), all obtained from the PEER database. Of these motions, the Loma Prieta Motion was selected and modified to match the target, site-specific, deterministic acceleration response spectrum at the project site (Harounian et al. 2014). The other motions were selected to evaluate the influence of different ground motion characteristics (i.e., in terms of intensity, frequency content, and duration) on the performance of the buried structures and their interaction with the surrounding soil.

The *desired* horizontal base motions were converted from prototype to model scale units and filtered to remove unwanted frequencies and to limit displacements to the stroke of the shaking table. These acceleration time histories were then double integrated to obtain displacement command signals. An iterative procedure similar to that described by Ketcham et al. (1991) was then implemented to obtain a command signal that produced a shaking table motion close to that *desired* both in terms of spectral accelerations and Arias Intensity time histories. The accelerations recorded on the shaking table and base of the container are referred to as *achieved* motions. The properties of the *achieved* base motions are summarized in Table 2 as recorded sequentially during a representative experiment, T-BL. Figure 3 shows the acceleration response spectra (5% damped) and Arias Intensity time histories of the base motions in T-BL. The *achieved* base motions varied slightly during different experiments because the weight and natural frequency of the model specimens were not the same, affecting the shake table performance. Therefore, the base motions are presented during each test when discussing results.

EXPERIMENTAL RESULTS

Acceleration Response

The presence of the model structure was expected to alter the accelerations at different elevations compared to far-field primarily due to kinematic interaction. The accelerations measured on the structure walls were compared to those measured in the far-field at the corresponding elevation. Figure 4 shows the spectral ratios of accelerations at the bottom, middle, and top of each model structure to those in the far-field in each test during three representative ground motions (Northridge L, M, and H). These ratios indicate whether accelerations were amplified or de-amplified due to the presence of the structure. The structure to far-field spectral ratios increased from the bottom of the structure to the top in all cases. The highest amplification of spectral ratios was observed at the top of the structure near the predominant frequency of the base motion (near 3 Hz).

As confining pressure increased, the movement of the buried structure was more controlled by the surrounding soil in terms of phase and amplitude. As shown in Figure *5* for a representative case (Northridge-H), the vibration of the structures were consistently in phase with the soil during all motions. This observation is consistent with the conclusions from numerical simulations presented by Murono and Nishimura (2000) when the structure fundamental frequency was greater than the effective fundamental frequency of the backfill soil, as is the case for all structures evaluated in this study.

Structure to far-field spectral ratios of near 1.0 were observed at elevations corresponding to the bottom and middle of the structure in all cases, meaning that the structure had a negligible impact on accelerations at these elevations (higher confining pressure) when compared to far-field. However, the top acceleration was amplified compared to the far-field, and its amplification was affected by the stiffness of the model structure. As the flexibility of the structure increased (i.e., going from T-Stiff to T-BL, and to T-Flexible), the degree of amplification increased. This is caused by a greater independent movement of the more flexible structure with respect to the surrounding soil at shallower depths (i.e., lower confinement).

Lateral Displacements

Racking displacement (Δ) is a critical seismic design parameter for buried box structures when shear waves propagate in a direction perpendicular to their longitudinal axis, distorting their cross-sectional shape (Anderson et al. 2008). Racking is described as the lateral displacement of the roof of the structure relative to its base. The peak racking displacement is often used to evaluate peak bending moments in a simple frame analysis of the 2D box structure.

In practice, the transverse racking of a box structure is often estimated using the NCHRP 611 guideline, which is based on the simplified method proposed by Wang (1993). In this simplified procedure, the structure racking is estimated indirectly from the deformations of the far-field soil and the stiffness of the structure relative to soil. The NCHRP 611 guideline is, however, based on the results of dynamic finite element analyses performed by Wang (1993) on buried box structures. The centrifuge experiments presented in this paper enabled us to experimentally evaluate the applicability of this guideline to the specific class of underground structures of interest.

The racking deformation time histories of the structure and far-field soil are shown in Figure 6 for one experiment and ground motion (T-Flexible, Northridge-L). The lateral displacement time histories were obtained by applying a band-pass, 5th order, a-causal, Butterworth filter with corner frequencies of 0.2 and 15 Hz, double integrating, and baseline correcting the accelerometer recordings on the structure (A12 and A14) and in the far-field at the elevations corresponding to the top and bottom of the structure (A2 and A4). Since no permanent deformation was measured on the buried structures with strain gauges, obtaining displacements indirectly from accelerometers was judged appropriate. The peak values of racking displacement on the structure ($\max|\Delta_{structure}|$) and far-field ($\max|\Delta_{FF}|$) were subsequently used to obtain the racking ratio ($R = \max|\Delta_{structure}|/\max|\Delta_{FF}|$) in each test and motion.

To calculate the flexibility of the structure relative to the far-field soil in accordance with the NCHRP 611 guidelines, the flexibility ratio, $F = (G_m.B)/(K_s.H)$, needed to be calculated, where G_m is the mean strain-compatible shear modulus of soil in the far-field, B is the structure width, K_s is the racking stiffness of the structure, and H is its height (Anderson et al. 2008). The far-field shear strain was calculated by dividing the corresponding racking displacement time history by the height of the structure (H), as shown in Figure 7. The normalized shear modulus (G_m/G_{max}) of the far-field soil at mid-depth of the structure (Darendeli 2001) was then evaluated at 65% of maximum far-field shear strain (Schnabel 1972) during each motion, an example of which is demonstrated in Figure 8. By using 65% of the peak shear strain, the goal was to roughly estimate the effective shear modulus of the far-field soil as opposed to its modulus at a single time corresponding to peak shear strain. The small-strain shear modulus of soil (G_{max}) was obtained at the mid-depth of the buried structure by using an empirical equation proposed by Bardet (1993) specifically for Nevada sand. Subsequently, the strain-compatible soil shear modulus (G_m) was calculated from G_m/G_{max} at the equivalent shear strain corresponding to each motion. Lastly, the K_s of each box structure was obtained from a standard frame analysis following the NCHRP 611 guideline.

The experimentally obtained values of racking versus flexibility ratio (R versus F) in T-Flexible, T-BL, and T-Stiff during all motions are compared with the numerically obtained NCHRP 611 guideline in Figure 9. The flexibility ratio (F) was shown to significantly influence the structure's transverse racking deformation both experimentally and numerically. The F values were near zero on the Stiff structure, implying a very stiff structure and negligible expected deformations according to NCHRP 611. The F values were less than 1.0 for the BL structure, implying a stiffer structure compared to the surrounding soil, hence less deformation. The Flexible structure with F values ranging from 0.5 to 2 during different motions implied a structure more flexible than the far-field soil, with the largest expected racking deformations. In general, the trends observed on the Flexible structure were consistent with the NCHRP 611 guideline, but NCHRP 611 overestimated the racking deformations slightly. Importantly, however, the NCHRP 611 procedure appeared to underestimate racking deformations on the stiffer structures (particularly the Stiff structure).

Lateral Earth Pressures

Tactile pressure sensors mounted on the south wall malfunctioned in T-BL and T-Stiff during some motions. Therefore, for consistency, only the pressure recordings obtained from tactile sensors mounted on the north wall of the three model structures are presented in this section. The sensors were conditioned and equilibrated prior to each test and they were calibrated both statically and dynamically, as discussed previously. To reduce scatter, the data obtained from nine sensels were averaged to represent a larger pressure area, as shown in Figure 10, after removing the nonworking sensels. After averaging the nine cells, the matrix of pressure time histories recorded was reduced from 28 rows × 14 columns (for two sensors) to 24 rows × 12 columns. Afterwards, the pressure time histories were averaged over the corresponding row to obtain one time history at a given depth (i.e., pressure matrix reducing to 24 rows × 1 column). This method was successful in reducing the scatter in pressure recordings, particularly when in contact with granular materials with local inhomogeneities (Gillis et al. 2015).

The dynamic increment of thrust was estimated by numerically integrating the dynamic pressure profile on the wall at each instance of time. The resulting dynamic thrust time histories estimated on three structures (BL, Flexible, and Stiff) during the Northridge-L motion are presented in Figure 11. The presented thrust time histories were subject to a band-pass, 5th order, a-causal, Butterworth filter with corner frequencies of 0.1 and 15 Hz, to remove low and high frequency noise that was sometimes present in the record and could affect the estimated peak dynamic thrust. As a result, the permanent change in thrust cannot be shown in this figure. From these time histories, however, the time corresponding to maximum dynamic thrust could be determined on each structure during each ground motion. Figure 12 shows the Fourier amplitude spectra of dynamic thrust on the three structures during the Northridge-L motion compared with that of acceleration at the mid-depth of structure walls (A13). This figure shows that the frequency content of dynamic thrust is similar to that of the acceleration recorded on the buried structure.

The static, pre-shake and post-shake lateral earth pressure and total (static and dynamic) pressure profiles at the time corresponding to maximum dynamic thrust on each structure are shown in Figure 13 during the Northridge-L event. These plots also include the theoretically expected range of static, at-rest (K_o conditions) and active (K_a) lateral earth pressures for comparison. A friction angle of 35° was assumed for Nevada sand at a relative density of 60% in these experiments (Popescu 1993). All three structures showed a reasonable trend in static earth pressure recordings. In most cases, static lateral earth pressures acting on the structure slightly increased after each shake, due to soil densification. The dynamic earth pressures at the time of maximum thrust were not negligible on any of the structures, even during the Northridge-L event with a base PGA of about 0.35g.

The dynamic increment of lateral earth pressures ($\Delta\sigma_E$) at the time of maximum thrust is shown in Figure 14 along with the predictions from the Mononobe-Okabe (M-O), Seed and Whitman (S-W), and Wood methods during three representative motions: Northridge-L, Northridge-M, and Northridge-H. The $\Delta\sigma_E$ values were estimated as the difference between total and pre-shake, static earth pressure recordings. The analytical methods were employed using 100% of the PGA recorded at the far-field soil surface (A4), for the purpose of this comparison. The M-O method provides indeterminate values of pressure at PGA values greater than 0.7g for a soil friction angle of 35°. Therefore, the M-O solution is not presented in Figure 14 during the Northridge-H motion. Wood's simplified procedure was once computed based on an L/H ratio of 1.5 corresponding to the centrifuge tests and once based on a larger L/H of 10 as an upper bound for comparison, where L is the lateral extent of the backfill soil and H the wall height. Wood's procedure does not take into account the increase of soil shear modulus with depth and therefore predicted large $\Delta\sigma_E$ values near the top of the wall.

The flexural rigidity of the buried structure significantly influenced the distribution or shape of the dynamic increment of pressure in a consistent manner. The $\Delta\sigma_E$ profile increased linearly with depth on the Flexible structure during all motions, while it followed a more rounded shape on the more rigid structures with its peak occurring closer to the center of the wall. Similar trends in the dynamic increment of earth pressure were observed in finite element analyses performed by Psarropoulos et al. (2005): as the flexural rigidity of the wall was increased from flexible to completely rigid, the shape of $\Delta\sigma_E$ profiles changed from triangular to a higher order polynomial. As shown in Figure 14, the $\Delta\sigma_E$ values measured on the Flexible structure roughly followed the M-O solution both in terms of shape and amplitude. This may have been due to the more flexible nature of this structure and its larger deformations (as confirmed by accelerometers and strain gauges). The more stiff structures (i.e., BL and Stiff) experienced $\Delta\sigma_E$ increments that fell between those predicted by M-O, S-W, and Wood's procedures. At shallower depths and lower confining pressures, the $\Delta\sigma_E$ increments were closer to M-O, while they fell between S-W and Wood's procedures near the bottom of the BL and Stiff structures.

The dynamic coefficient of lateral earth pressure (ΔK_E) was calculated for an equivalent triangular dynamic earth pressure profile by dividing the actual dynamic thrust by $\gamma H^2/2$, where γ is the unit weight of backfill soil and H the wall height. The equivalent ΔK_E values obtained experimentally at the time of maximum thrust on all three structures as a function of the PGA of far-field surface motion (A4) are shown in Figure 15. This figure also includes the results obtained from previous centrifuge experiments performed by Mikola (2012) on a model basement structure (more flexible than those considered in this study) as well as the predictions from the M-O, S-W, and Wood methods for comparison. The ΔK_E values obtained in all experiments generally increased with increasing PGA. The experiments performed by Mikola (2012) indicated that the S-W method could serve as an upper-bound method for dynamic lateral earth pressures. This conclusion was not valid in all cases for the specific class of underground structures of interest in this study (*stiff-unyielding*): the dynamic earth pressures acting on the BL and Flexible structures were in line with those of Mikola (2012), being either close to or smaller than the S-W method; but dynamic earth pressures acting on the Stiff structure often exceeded the S-W method and approached Wood's procedure. It must be noted, however, that the reliability of pressure sensors is a topic of ongoing research, and therefore it is important to evaluate bending strains in parallel with numerical simulations before drawing definite conclusions on pressure trends.

Figure 16 shows the centroid of the dynamic increment of pressure ($\Delta\sigma_E$) measured at the time of maximum thrust on all three structures against the PGA of the far-field surface motion (A4). The centroid was calculated by fitting the dynamic increment of pressure at the time of maximum thrust with a polynomial that was extrapolated to the entire height of the wall. The plot also includes the centroids derived from the M-O, S-W, and Wood methods for comparison. The depth of dynamic pressure centroid did not appear to be significantly affected by shaking intensity (e.g., PGA), but was influenced by the structure's stiffness. The depth of dynamic pressure centroids on the Flexible structure followed closely the M-O method (as expected based on the trends in Figure 14). The dynamic pressure centroid depths on the BL and Stiff structures generally fell between those predicted by the M-O, S-W, and Wood methods.

Bending Strains and Moments

Bending strains were measured on both walls before, during, and after each ground motion. Only strains from the south wall are presented because some of the sensors on the north wall malfunctioned. The deformation patterns, however, were expected and confirmed to be symmetric. Dynamic bending strain ($\Delta\varepsilon_E$) profiles are presented at the time of maximum strain or moment during each motion in Figure 17. Because the tactile sensors had a different data acquisition system, to avoid uncertainties associated with time synchronization of different sensors, the dynamic strain profiles are shown at the time one of the strain gauges recorded maximum strain on that wall, as opposed to the time of maximum thrust used in the previous section.

The measured $\Delta\varepsilon_E$ values generally increased as shaking intensity increased. The distribution and amplitude of $\Delta\varepsilon_E$ profiles varied greatly among the three structures. The amplitude of $\Delta\varepsilon_E$ was proportional to the structure's flexibility, as expected. The distribution of $\Delta\varepsilon_E$ was approximately linear on the Flexible structure, and transitioned to a higher order polynomial on stiffer structures (BL and Stiff structures). The dynamic increment of bending moments (ΔM_E) at the same time were subsequently calculated from the corresponding strain values, as shown in Figure 18. Eventhough the $\Delta\varepsilon_E$ profiles were significantly smaller on stiffer structures, in most cases ΔM_E slightly increased as the structure's flexural stiffness increased, because bending moments take into account the wall's moment of inertia. The distribution of ΔM_E changed from approximately linear to a higher order polynomial as the structure stiffness increased, a trend consistent with the $\Delta\sigma_E$ distributions.

CONCLUDING REMARKS

Traditionally, underground structures are categorized either as *yielding* or *rigid-unyielding*, and designed using simplified analytical methods that were developed for one of these two extreme conditions. Underground reservoir structures of interest in this study fall in neither of these categories, because they are not fully rigid, but their wall deformation is limited as they are stiff and restrained at their base and roof (in this paper classified as *stiff-unyielding* structures). The kinematic constraints of these structures are not fully captured by simplified seismic procedures, and advanced numerical tools have not been calibrated or validated adequately against physical model studies. SSI effects near these structures depend on foundation fixity, properties of the surrounding soil, flexibility of the structure relative to soil, and the characteristics of the earthquake motion. In this paper, we present the results of three centrifuge experiments that investigate the seismic response of *stiff-unyielding* buried reservoir structures in medium dense, dry sand and the influence of structure stiffness and characteristics of the earthquake motion on accelerations, racking deformations, lateral earth pressures, and bending strains and moments. The primary conclusions of this paper are as follows:

1. The acceleration response of the box structure with respect to the far-field was influenced by the confining pressure in soil and the flexural rigidity of the structure. The structure to far-field spectral ratios increased from the bottom of the structure to the top during all motions. As the confining pressure increased, the movement of the buried structure was more controlled by the inertia of the surrounding soil. The highest amplification of spectral ratios was observed at the top of the more flexible structure near the predominant frequency of the base motion.
2. Peak racking deformations measured on the box structures increased as the structural flexibility increased compared to the far-field soil. The NCHRP 611 guideline was observed to be more appropriate for flexible structures, but importantly, it underestimated racking displacements for stiffer underground box structures during all motions.

3. The flexural rigidity of the box structure was shown to affect the distribution of dynamic earth pressures ($\Delta\sigma_E$) measured during different motions. The most flexible structure experienced a triangular distribution of $\Delta\sigma_E$, similar to those predicted by the M-O method, while the stiffer structures displayed a higher order polynomial distribution.
4. The experimentally obtained equivalent dynamic coefficients of lateral earth pressure (ΔK_E) at the time of maximum thrust increased with increasing ground motion intensity (e.g., PGA) in most cases. The ΔK_E values on the more flexible structures (BL and Flexible) were in line with previous experiments conducted on relatively flexible basement walls and were either close to or smaller than those predicted by the S-W method. The ΔK_E values on the Stiff structure, however, often exceeded the predictions of the S-W method and approached those of Wood's.
5. The centroid of the dynamic earth pressures ($\Delta\sigma_E$) at the time of maximum thrust did not appear to be affected by the intensity of shaking (e.g., PGA), but was influenced by the flexural stiffness of the structure. The estimated centroid locations on the Flexible structure were close to the M-O predictions, and the centroid locations on the BL and Stiff structures generally fell between those predicted by M-O, S-W, and Wood's methods.
6. Dynamic bending moments (ΔM_E) at the time of maximum thrust slightly increased with increasing structural flexural stiffness. Further, the distribution of ΔM_E changed from approximately linear to a higher order polynomial as the structure stiffness increased, a trend similar to the $\Delta\sigma_E$ profiles.

Comparing the experimental results with methods commonly used to evaluate the performance of underground and retaining structures identifies the following key points:

- None of the existing methods adequately capture the structural loading and deformations across the entire range of stiffness and ground motions in which critical underground facilitates must be designed.
- The analysis procedures are not consistently conservative or unconservative with respect to seismic design.
- There is insufficient guidance in practice on how to select different methods for different classes of underground structures, especially for s*tiff-unyielding* structures. As a result, there is a need for improved methodologies and guidance for design of underground structures.

The presented experimental results are intended to provide important insights into the influence of structure stiffness and ground motion properties on seismic forces as well as the seismic performance of an entire class of *stiff-unyielding* buried structures with translational and rotational restraints at the top and bottom. Additionally, parallel nonlinear numerical simulations are necessary before the results can be used to provide general and definite recommendations for practice.

ACKNOWLEDGMENTS

The authors would like to thank the Los Angeles Department of Water and Power (LADWP) for financial support of this research.

REFERENCES

Al Atik, L. and Sitar, N. (2010), "Seismic earth pressures on cantilever retaining structures," *Journal of Geotechnical and Geoenvironmental Engineering*, October, (136) 10, pp. 1324-1333.

Andersen, G.R., Whitman, R.V., & Germaine, J.T. (1991). “Seismic response of rigid tilting walls.” *Centrifuge 91*, H.Y. Ko and F.G. McLean, eds., Balkema, Rotterdam, The

Netherlands, 417–423.

Anderson, D.G., Martin, G.R., Lam, I.P. and Wang, J.N. (2008). *Seismic design and analysis of retaining walls, buried structures, slopes and embankments*, *NCHRP Report 611*. Transportation Research Board, National Cooperative Highway Research Program, Washington, D.C.

Bardet, J. P., Huang, Q., & Chi, S. W. (1993). "Numerical prediction for model no. 1." *Proceedings of the International Conference on the Verification of Numerical Procedures for the Analysis of Soil Liquefaction Problems* (Vol. 1, pp. 67-86). Balkema, Netherlands.

Bolton M.D. and Steedman, R.S. (1982). "Centrifugal testing of micro-concrete retaining walls subject to base shaking," *Proceedings of Conference on Soil dynamics and Earthquake Engineering*, Southampton, 311-329, Balkema, Rotterdam.

Cilingir, U., and Madabhushi, S. G. (2011). "Effect of depth on the seismic response of square tunnels," *Soils and foundations*, *51*(3), 449-457

Darendeli, M. B. (2001). *Development of a new family of normalized modulus reduction and material damping curves*. PhD Dissertation, Univ. of Texas at Austin, Austin, TX.

Dashti, S., Gillis, K., Ghayoomi, M., and Hashash, Y. (2012). "Sensing of lateral seismic earth pressures in geotechnical centrifuge modeling." *Proceedings of 15th World Conf. on Earthquake Eng.*, Lisbon, Portugal.

Davis, C.A. (2003). "Lateral seismic pressures for design of rigid underground lifeline structures." *Proceedings of the 6th U.S. Conference on Lifeline Earthquake Engineering*, ASCE. 1001-1010.

Derrick, T.R. (2004). "Signal Processing. In: Research Methods for Biomechanics." Chapter 11, Robertson, D.G.E., Hamill, J. Caldwell, G.E., Kamen, G. (eds). Human Kinetics Publishers, Champaign, IL, pp. 227-238.

Dewoolkar, M.M., Ko, H. and Pak R.Y.S. (2001). "Seismic behavior of cantilever retaining walls with liquefiable backfills." *Journal of Geotechnical and Geoenvironmental Engineering, ASCE*, (127) 5, 424-435.

Ebeling, M.E. and Morrison, E.M. (1992). "The seismic design of waterfront retaining structures," *Technical Report ITL-92-11*. U.S. Army Corps of Engineers, Washington, D.C.

Ghayoomi, M., Dashti, S., & McCartney, J. S. (2013). "Performance of a transparent Flexible Shear Beam container for geotechnical centrifuge modeling of dynamic problems". *Soil Dynamics and Earthquake Engineering*, *53*, 230-239

Ghayoomi, M., Dashti, S., McCartney, J.S. (2012). "Effect of boundary conditions on the performance of a transparent flexible Shear Beam-type container," *2nd International Conference on Performance.-Based Design Earthquake Geotechnical Engineering.* Taormina, Italy.

Gillis, K., Dashti, S., and Hashash, Y. (2015). "Dynamic calibration of tactile sensors for measurement of soil pressures in centrifuge." *ASTM Geotechnical Testing Journal*, 38(3): 261–274.

Harounian, A., Davis, C. A., Lew, M., and Hudson, M. B. (2014). "Beyond code-based design: Use of advanced numerical modeling to support design of Los Angeles's Headworks Reservoir," *Proceedings of the 2014 Geo-Congress*, Atlanta, GA, Feb 23–26, ASCE, Reston, VA, pp. 475–484.

Hradilek, P. J. (1972). "Behavior of underground box conduits in the San Fernando Earthquake of 9 February 1971," Report No. TR-E-72-1, U.S. Army Corps of Engineers, Los Angeles

Ketcham, S. A., Ko, H. Y., and Sture, S. (1991). ‘‘Performance of an earthquake motion simulator for a small geotechnical centrifuge.'' *Centrifuge 91*, H. Y. Ko and F. G. McLean, eds., Balkema, Rotterdam, The Netherlands, 361–368.

Ko, H. Y. (1988). ''The Colorado centrifuge facility.'' *Centrifuge 88*, J. F. Corte, ed., Balkema, Rotterdam, The Netherlands, 73–75.

Lew, M., Sitar, N., Al Atik, L., Pourzanjani, M. and Hudson, M.B. (2010). "Seismic earth pressures on deep building basements," *Structural Engineers Association of California, Proceedings of the Annual Convention, 2010*.

Mikola, R. (2012). "Seismic earth pressures on retaining structures and basement walls in cohesionless soils," *PhD Thesis*, University of California, Berkeley, CA.

Mononobe, N. and Matsuo M. (1929). "On the determination of earth pressures during earthquakes," *Proc. World Engineering Congress*, Vol. 9, 179-187.

Murono, Y., & Nishimura, A. (2000). "Evaluation of seismic force of pile foundation induced by inertial and kinematic interaction," *Proc. of 12th World Conference on Earthquake Engineering* (No. 1496).

Nakamura, S. (2006). "Reexamination of Mononobe-Okabe theory of gravity retaining walls using centrifuge model tests," *Soils and Foundations*, (46) 2, 135-146.

Okabe S. (1926). "General theory of earth pressure," *Journal of the Japanese Society of Civil Engineers*, Tokyo, Japan, (12)

Olson, S.M., Hashash, Y.M.A., Muszynski, M.R., Phillips, C., and Polito, C. (2011). "Using tactile pressure sensors to measure lateral spreading-induced earth pressures against a large, rigid foundation," *Fifth Int'l Conf. on Recent Advances in Geotechnical Earthquake Engineering and Soil Dynamics*. S. Prakash (Ed.), San Diego, CA.

Ortiz, L. A., Scott, R. F., & Lee, J. (1983). "Dynamic centrifuge testing of a cantilever retaining wall." *Earthquake Engineering & Structural Dynamics*, 11(2), 251-268.

Ostadan, F. (2005). "Seismic soil pressure for building walls: An updated approach." *Soil Dynamics and Earthquake Engineering*, *25*(7), 785-793.

Popescu, R., & Prevost, J. H. (1993). "Centrifuge validation of a numerical model for dynamic soil liquefaction." *Soil Dynamics and Earthquake Engineering*, 12(2), 73-90.

Psarropoulos, P. N., Klonaris, G., and Gazetas, G. (2005). "Seismic earth pressures on rigid and flexible retaining walls." *Int. J. Soil Dyn. Earthquake Eng.*, 25, 795–809.

Richards, R., Huang, C. and Fishman, K.L. (1999). "Seismic earth pressure on retaining structures," *Journal of Geotechnical and Geoenvironmental Engineering*, ASCE, 125(9): 771–778.

Roth, W.H. and Mehrain, M. (2010). "The meaning of seismic earth pressure." *Annual SEAOC Convention.*

Seed, H.B. and Whitman, R.V. (1970). "Design of earth retaining structures for dynamic loads," *ASCE Specialty Conference, Lateral Stresses in the Ground and Design of Earth Retaining Structures,* Cornell Univ., Ithaca, New York, 103–147.

Stadler, A. T. (1996). "Dynamic centrifuge testing of cantilever retaining walls," *Ph.D. Thesis*. Univ. of Colorado at Boulder, Boulder, Colo.

Steedman, R. S., and Zeng, X. (1991). "Centrifuge modeling of the effects of earthquakes on free cantilever walls". Centrifuge'91.

Tessari, A., Abdoun, T., Sasanakul, I., and Wroe, E. (2014). "Boundary corrected calibration of tactile pressure sensors," *Physical Modelling in Geotechnics*, 331 -336.

Tsinidis, G., Pitilakis, K., Madabhushi, G., and Heron, C. (2015). "Dynamic response of flexible square tunnels: centrifuge testing and validation of existing design methodologies."

Geo-technique, 65(5), 401-417

Veletsos, A. S., and A. H. Younan (1994b) “Dynamic modeling and response of soil-wall systems,” *Journal of Geo. Engr.*, ASCE, Vol. 120, No. 12, pp. 2155-2179.

Wang, J.N. (1993). “Seismic Design of Tunnels: A State-of-the-Art Approach,” Monograph 7. New York, NY: Parsons Brinckerhoff Quade & Douglas, Inc.

Wood, J.H. (1973). “Earthquake induced soil pressures on structures,” *PhD Thesis*, California Institute of Technology, Pasadena, CA.

Zhai, E., Davis, C.A., Yan, L., Hu, J. (2013). “Numerical simulations of geotechnical centrifuge Modeling of seismic earth pressures on an underground restrained structure,” *International Efforts in Lifeline Earthquake Engineering*. ASCE. December 2013, 369-376.

List of Figure Captions

Figure 1. Instrumentation layout in experiments T-BL, T-Flexible, and T-Stiff (dimensions in prototype scale meters).

Figure 2. Elevation view of model specimen in experiment T-BL.

Figure 3. (a) Acceleration response spectra (5% damped) and (b) Arias Intensity time histories of the achieved base motions in T-BL.

Figure 4. Spectral ratio (5% damped) of structure to far-field accelerations in three tests (T-BL, Flexible, Stiff) during the Northridge-L, Northridge-M, and Northridge-H motions.

Figure 5. Acceleration time histories in the middle of the structure and at the corresponding depth within the far-field soil in T-Flexible, T-BL, and T-Stiff during the Northridge-H motion.

Figure 6. Structure and far-field racking displacement time histories in T-Flexible during the Northridge-L motion.

Figure 7. Lateral displacement and shear strain time histories in the far-field in T-Flexible during the Northridge-L motion.

Figure 8. The modulus reduction (Darendeli 2001) curve used to calculate G_m of soil in the far-field in T-Flexible during the Northridge-L motion.

Figure 9. Experimental racking vs. flexibility ratios of three structures during different ground motions as compared to the NCHRP 611 guideline.

Figure 10. Schematic of tactile pressure sensor cell averaging.

Figure 11. Dynamic thrust time histories on the structures in T-Flexible, T-BL, and T-Stiff compared to the container base motion during the Northridge-L motion.

Figure 12. Fourier amplitude spectra of dynamic thrust and mid-depth acceleration (A13) recorded on the structure in T-Flexible, T-BL, and T-Stiff during the Northridge-L motion.

Figure 13. Static and total (static and dynamic) pressure profiles measured by tactile pressure sensors at the time of maximum thrust in T-Flexible, T-BL, and T-Stiff during the Northridge-L motion.

Figure 14. Dynamic pressure ($\Delta\sigma_E$) profiles at the time of maximum thrust measured by tactile pressure sensors on three structures (BL, Flexible, Stiff) compared to the M-O, S-W, and Wood methods.

Figure 15. Dynamic coefficient of lateral earth pressure (ΔK_E) at the time of maximum thrust as a function of far-field surface PGA in T-BL, T-Flexible, and T-Stiff compared with analytical procedures and previous centrifuge experiments performed by Mikola (2012) on a basement wall.

Figure 16. Centroid of dynamic increment of pressure at the time of maximum thrust as a function of far-field surface PGA in T-BL, T-Flexible, and T-Stiff compared with analytical procedures.

Figure 17. The dynamic increment of bending strains ($\Delta\varepsilon_E$) on the walls of three structures (BL, Flexible, Stiff) at the time of maximum moment during the Northridge-L, Northridge-M, and Northridge-H motions.

Figure 18. The dynamic increment of bending moments (ΔM_E) on the walls of three structures (BL, Flexible, Stiff) at the time of maximum moment during the Northridge-L, Northridge-M, and Northridge-H motions.

Table 1. Dimensions and properties of model structures used in centrifuge (prototype scale).

Structure	Height & Width (m) (Outer Edge to Outer Edge)	Thickness			Lateral Stiffness, K_L (kN/m/m)	Fundamental Frequency (Hz)	
		Base (m)	Roof (m)	Walls (m)		Numerical	Experimental
Baseline (BL)	10.5 & 12.1	0.69	0.37	0.56	31,500	4.0	3.9
Flexible		0.50	0.28	0.28	6,115	2.0	1.9
Stiff		1.46	1.12	1.13	472,518	9.9	9.1

Note: Model structures were 17.46 m long (approximately equal to the inside width of the centrifuge container).

Table 2. Base motion properties as recorded in T-BL (all units in prototype scale).

Ground Motion Name	**PGA (g)**	**Arias Intensity I_a (m/s)**	**Significant Duration $D_{5\text{-}95}$ (s)**	**Mean Frequency f_m (Hz)**	**Predominant Frequency f_p (Hz)**
Northridge-L	0.36	1.6	15.4	1.41	2.86
Northridge-M	0.81	5.4	19.5	1.52	3.57
Northridge-H	1.20	11.6	25.1	1.59	3.57
Izmit	0.33	2.1	39.5	1.79	4.17
Loma	1.00	12.4	13.3	2.00	3.70

Figure

Click here to download Figure Figure 1.tif

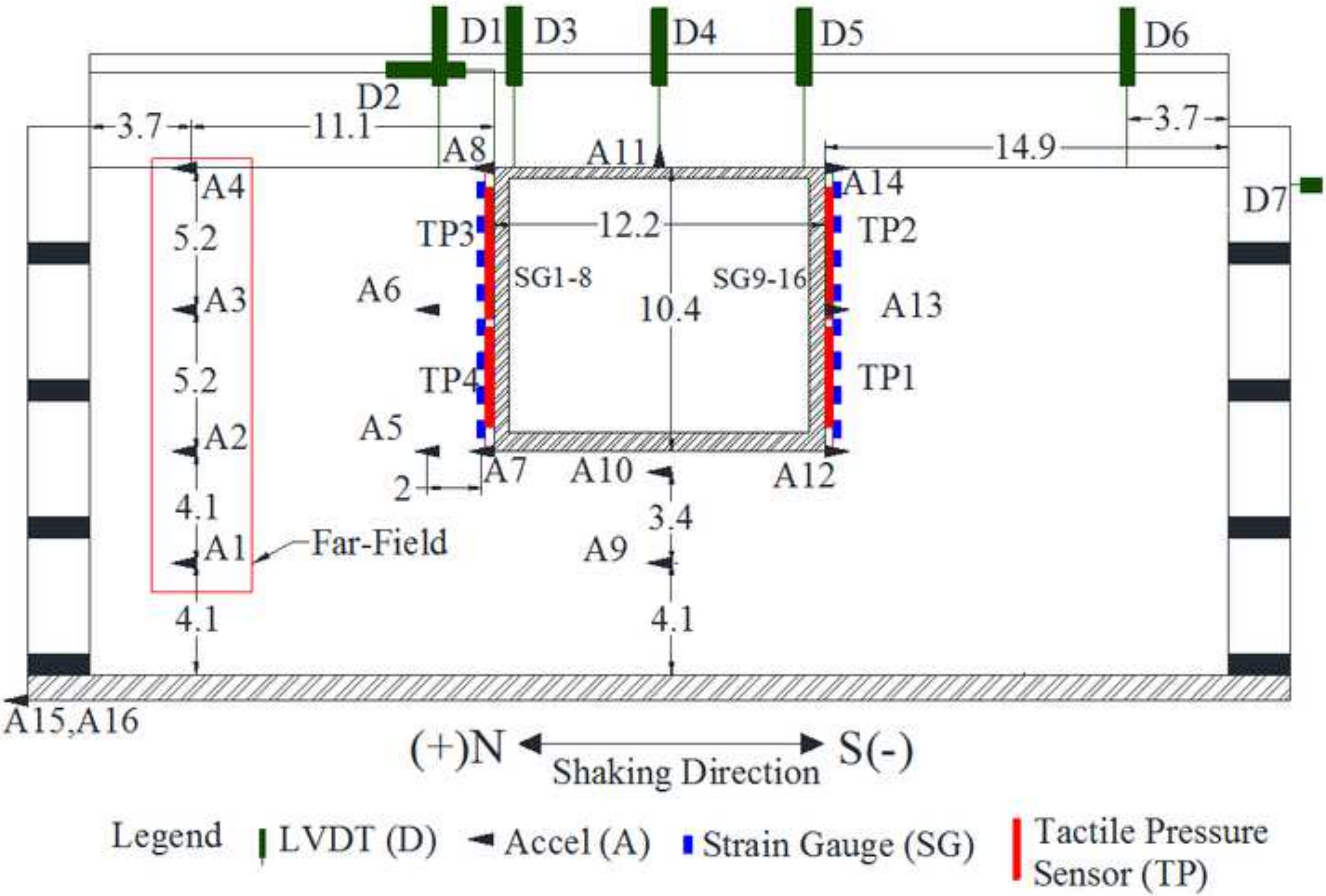

Figure

Click here to download Figure Figure 2.tif

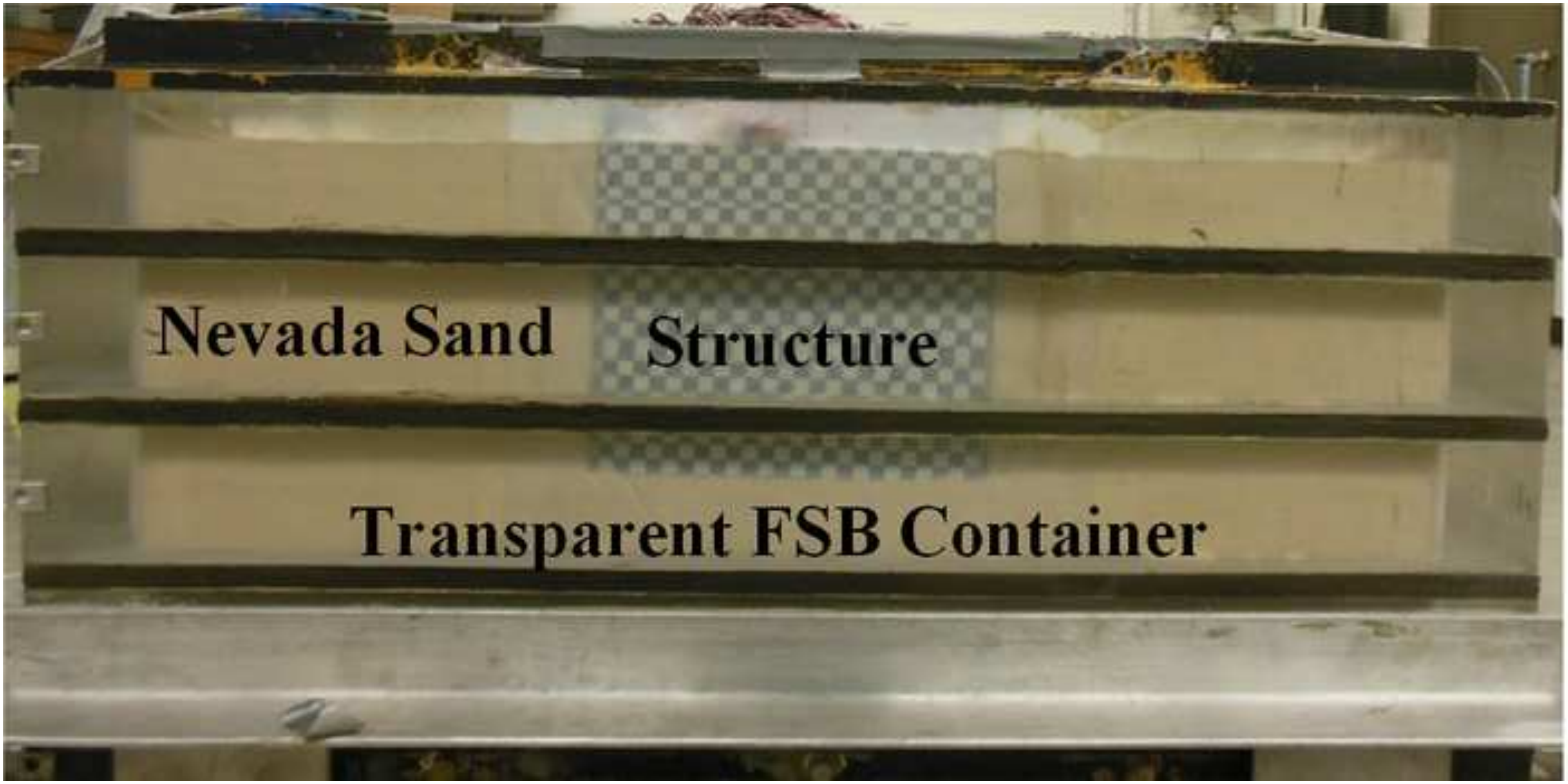

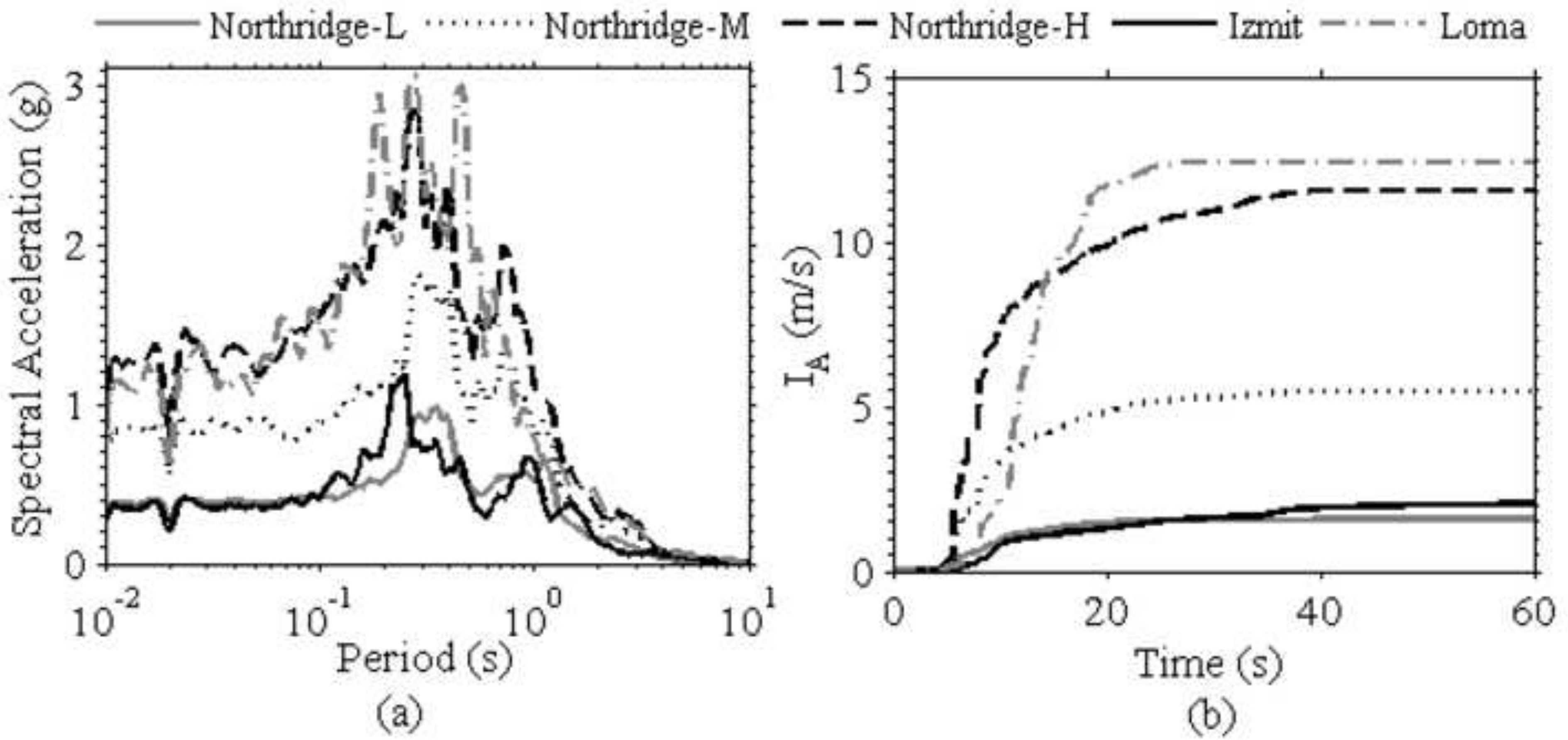

Northridge-L
Northridge-M
Northridge-H
Izmit
Loma
Spectral Acceleration (g)
0
1
2
3
10^{-2}
10^{-1}
10^{0}
10^{1}
Period (s)
(a)
I_A (m/s)
0
5
10
15
0
20
40
60
Time (s)
(b)

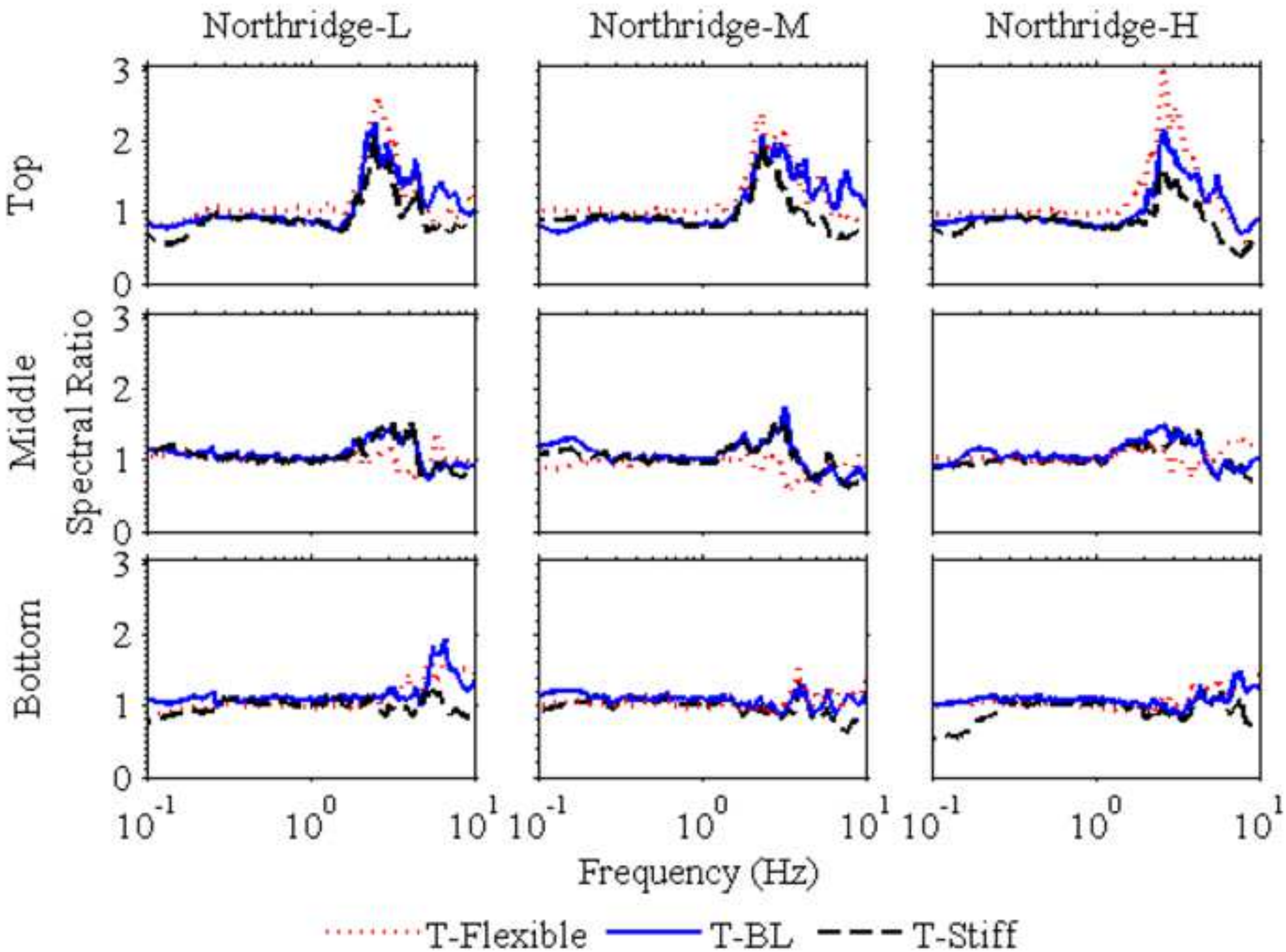

Northridge-L
Northridge-M
Northridge-H
Top
Middle
Bottom
Spectral Ratio
0
1
2
3
10^-1
10^0
10^1
Frequency (Hz)
T-Flexible
T-BL
T-Stiff

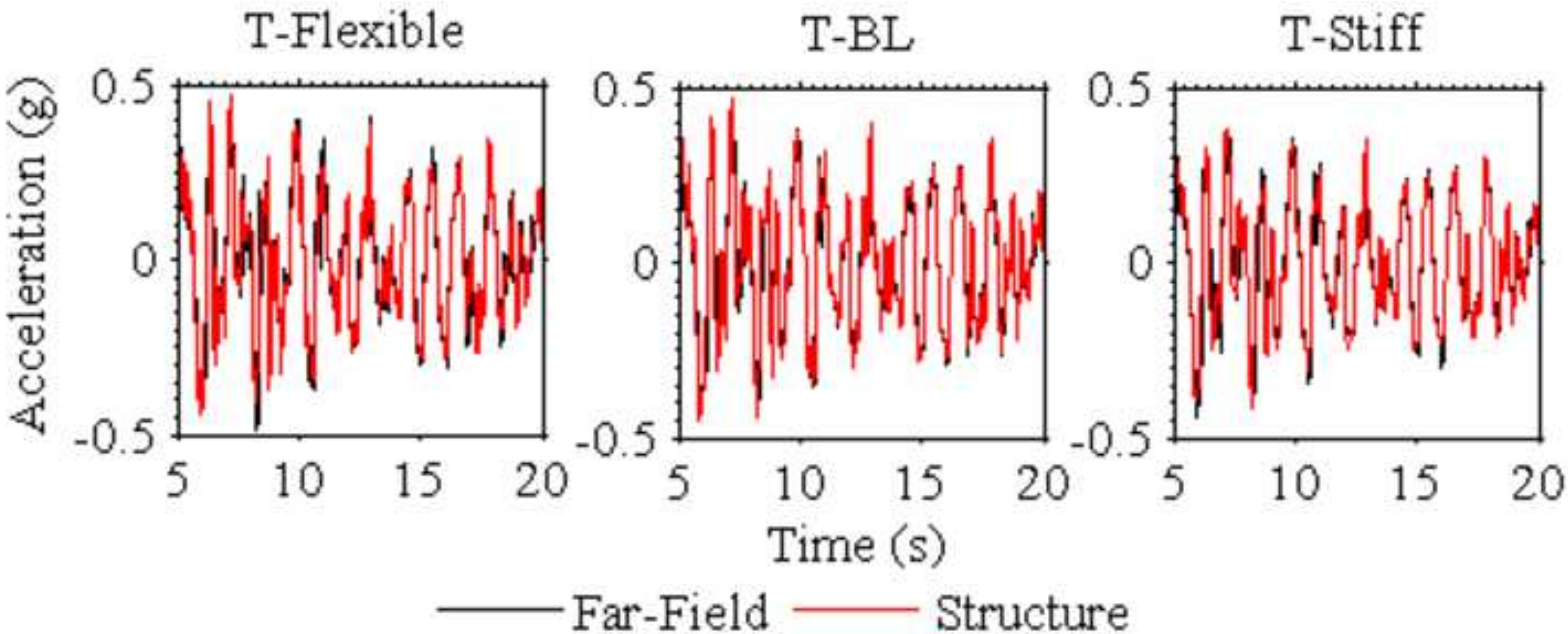
T-Flexible
T-BL
T-Stiff
Acceleration (g)
0.5
0
-0.5
5
10
15
20
Time (s)
Far-Field
Structure

Figure

Click here to download Figure Figure 6.tif

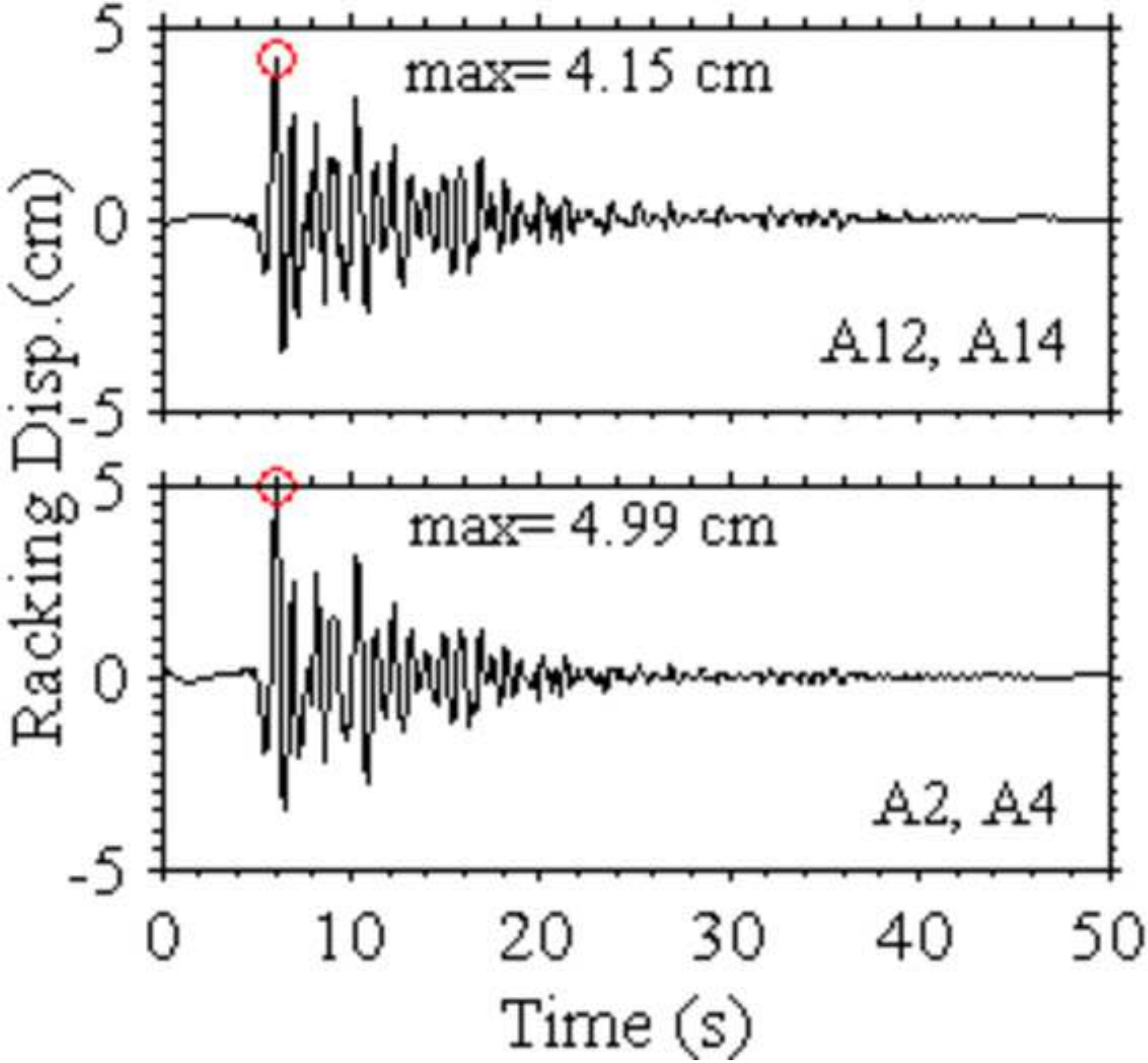

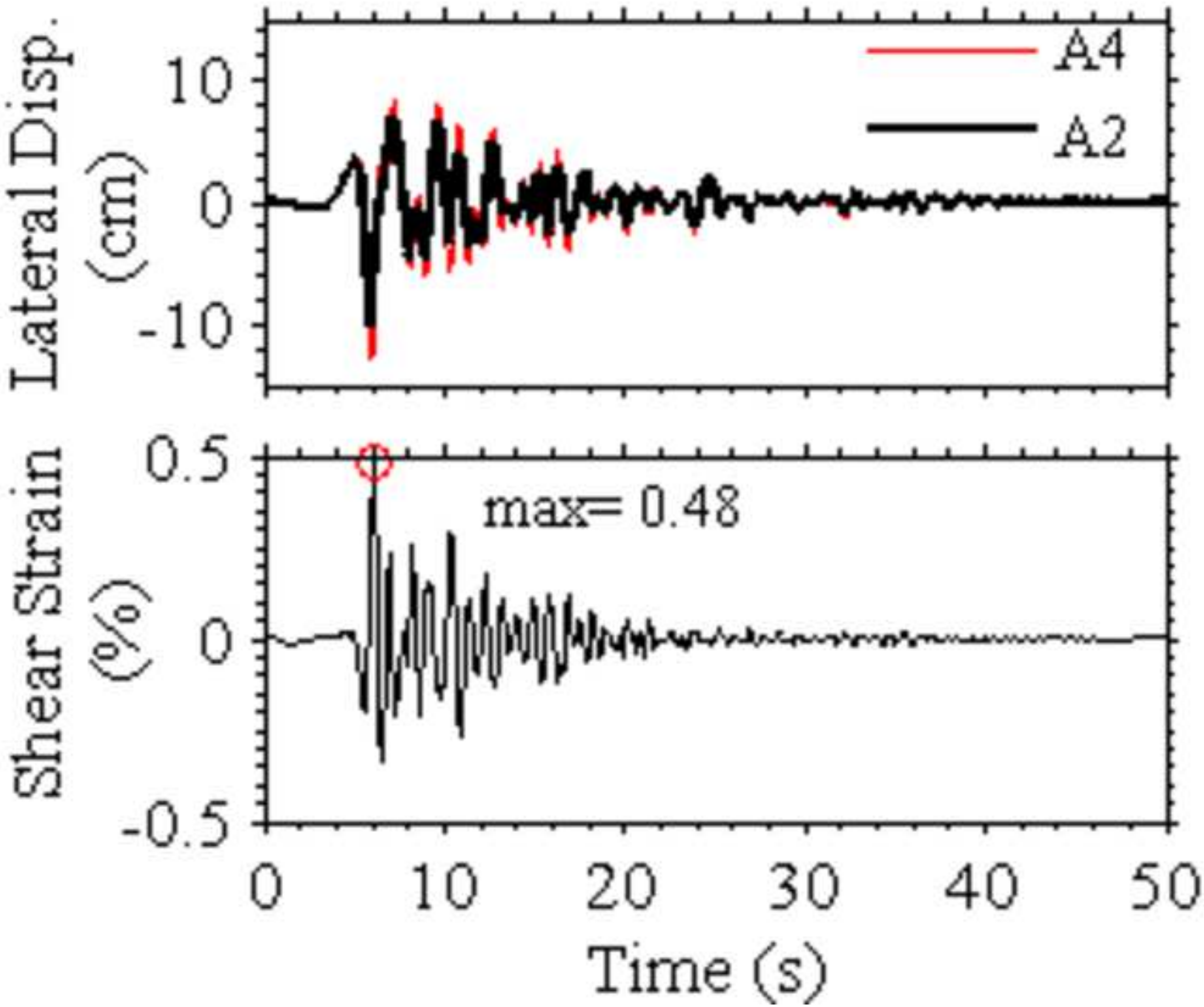
Lateral Disp. (cm)
10
0
-10
A4
A2
Shear Strain (%)
0.5
0
-0.5
max= 0.48
0
10
20
30
40
50
Time (s)

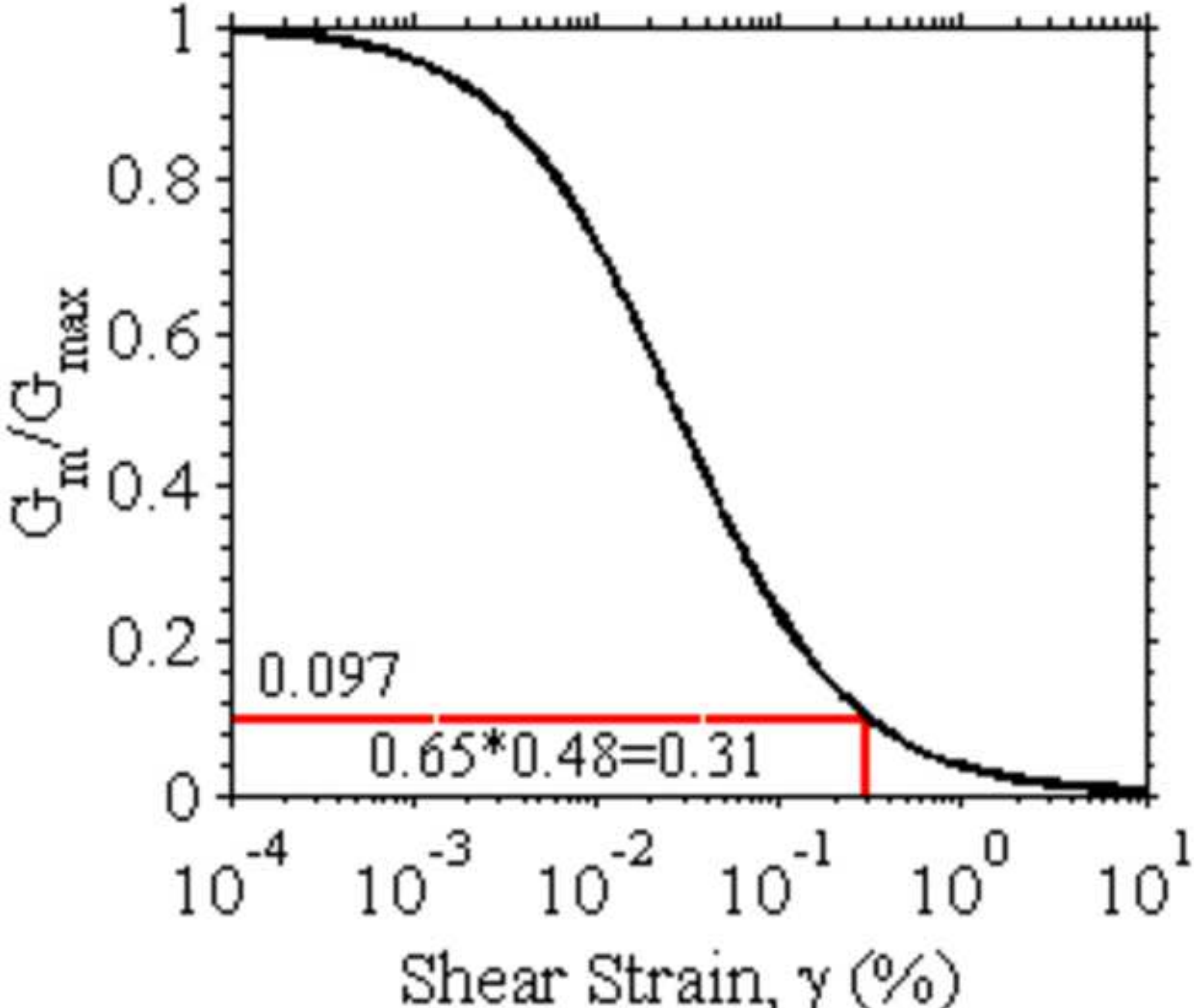

1
0.8
0.6
0.4
0.2
0
Gm/Gmax
0.097
0.65*0.48=0.31
10-4
10-3
10-2
10-1
100
101
Shear Strain, γ (%)

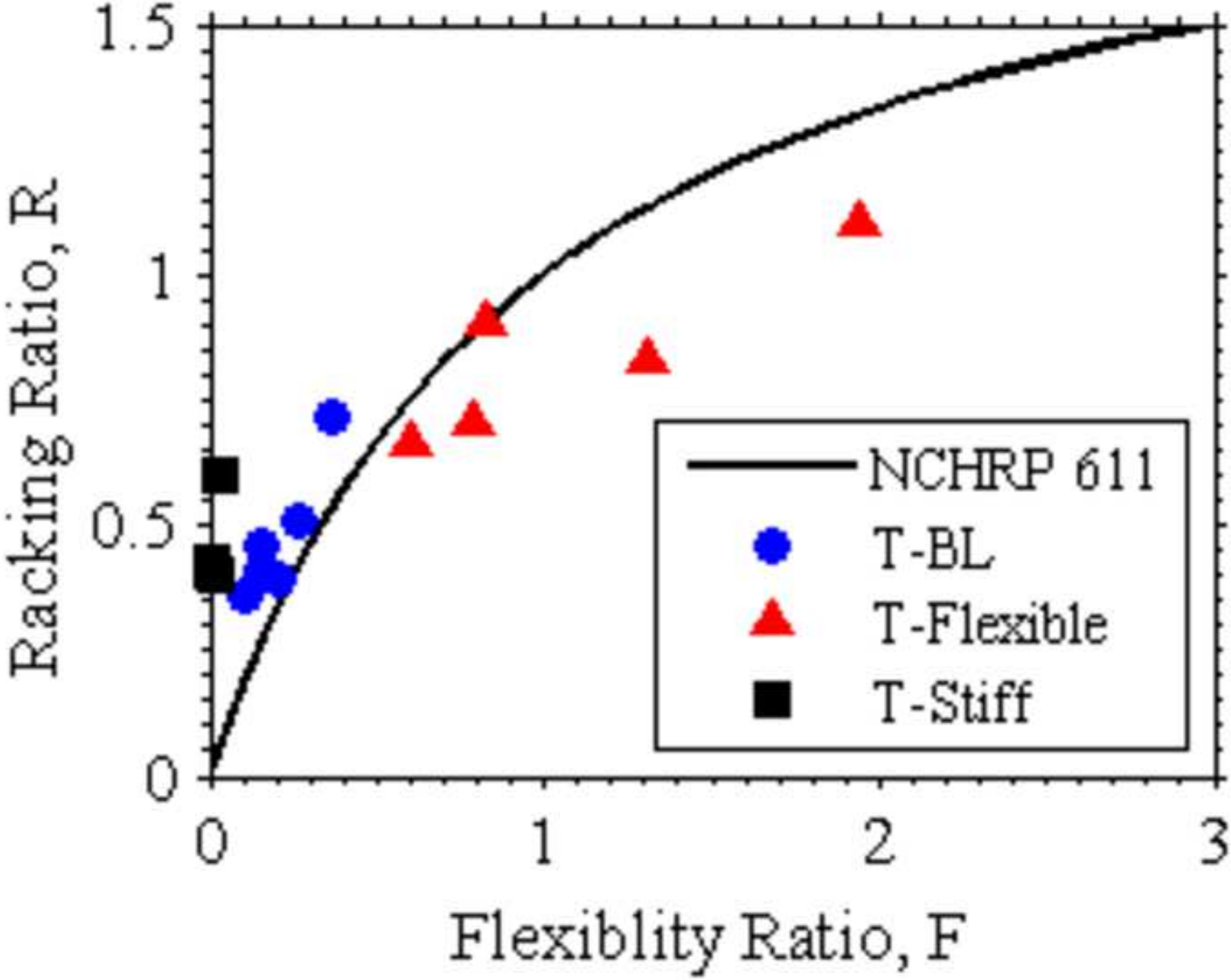
1.5
1
0.5
0
0
1
2
3
Racking Ratio, R
Flexiblity Ratio, F
NCHRP 611
T-BL
T-Flexible
T-Stiff

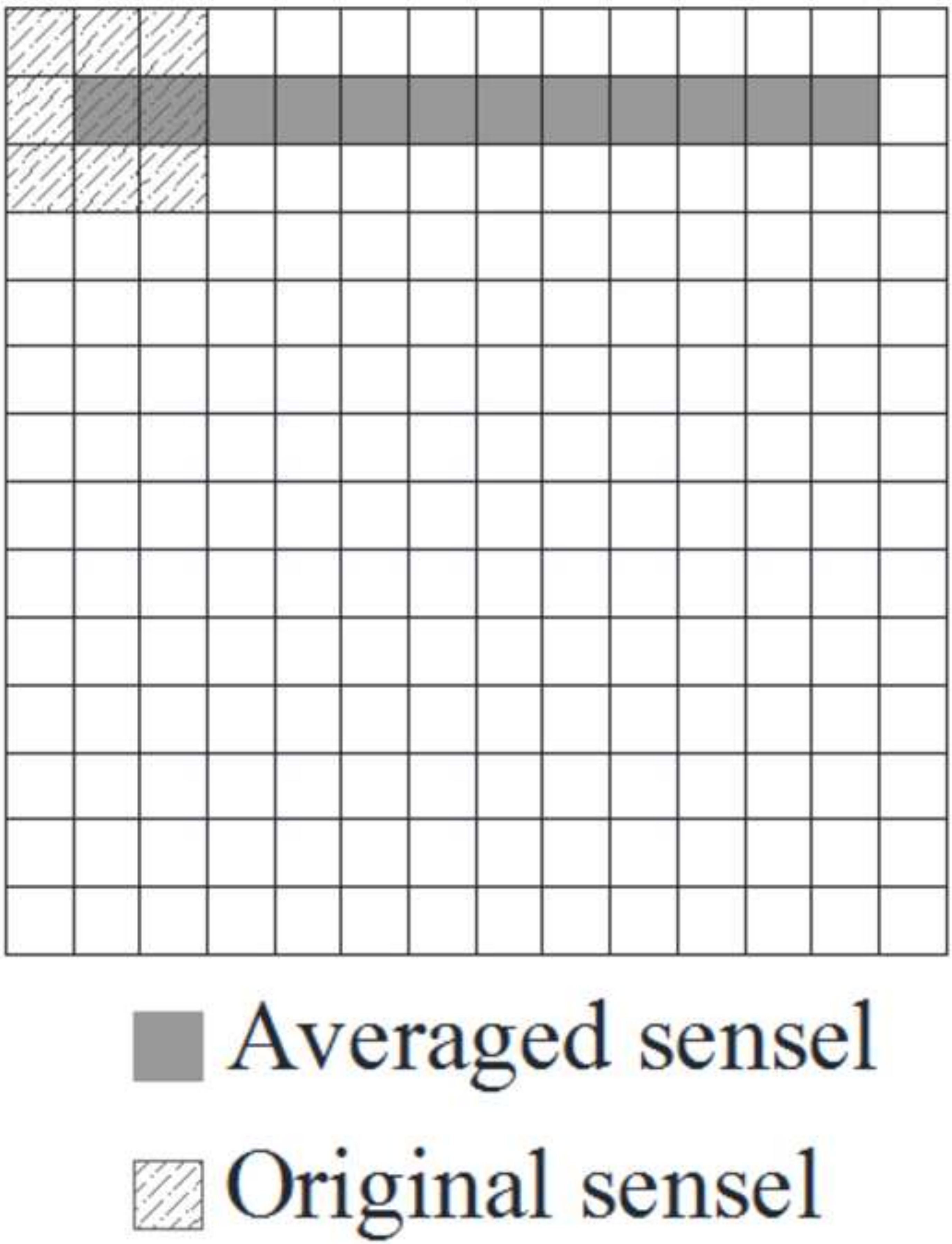
Averaged sensel
Original sensel

Figure Click here to download Figure Figure 11.tif

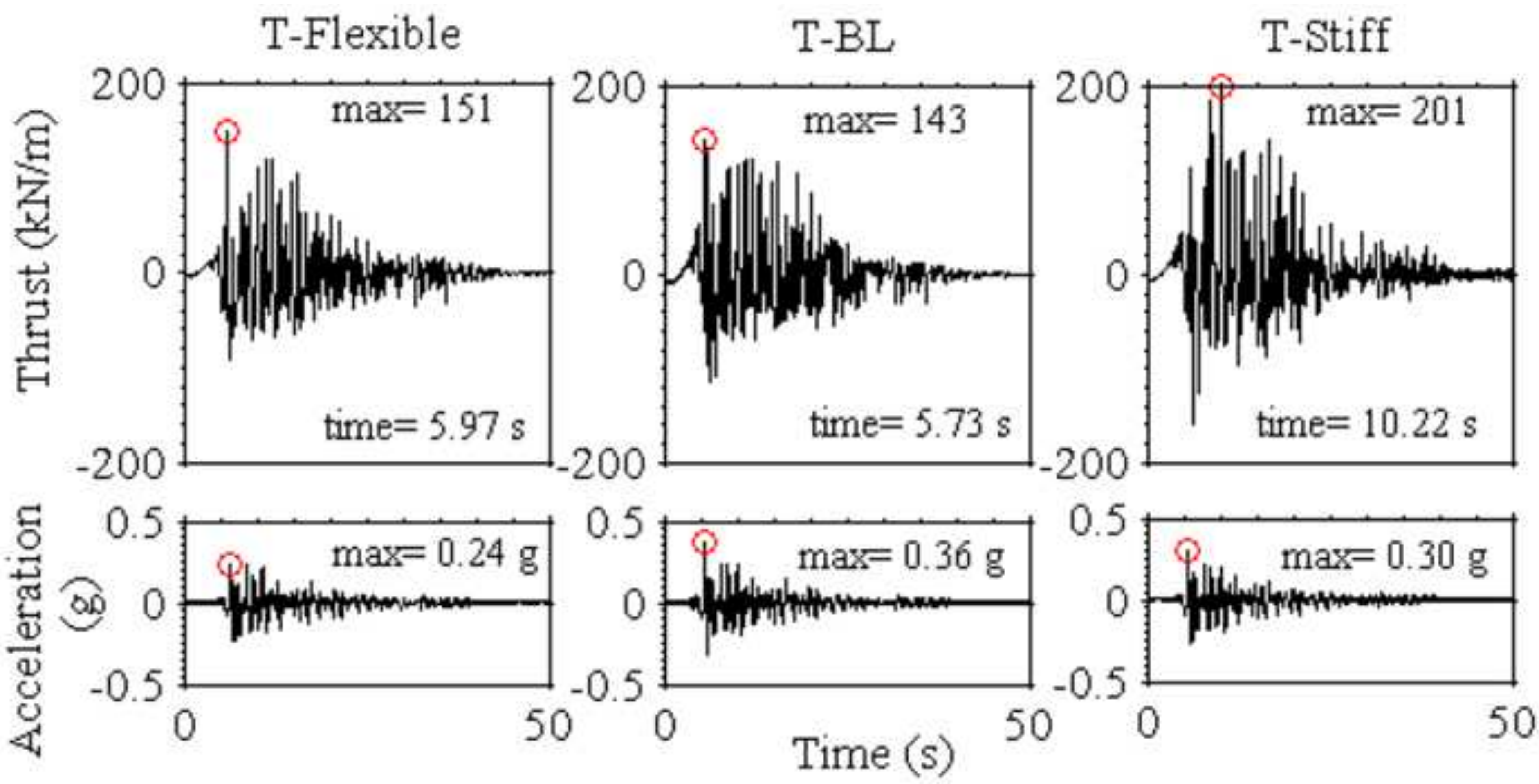

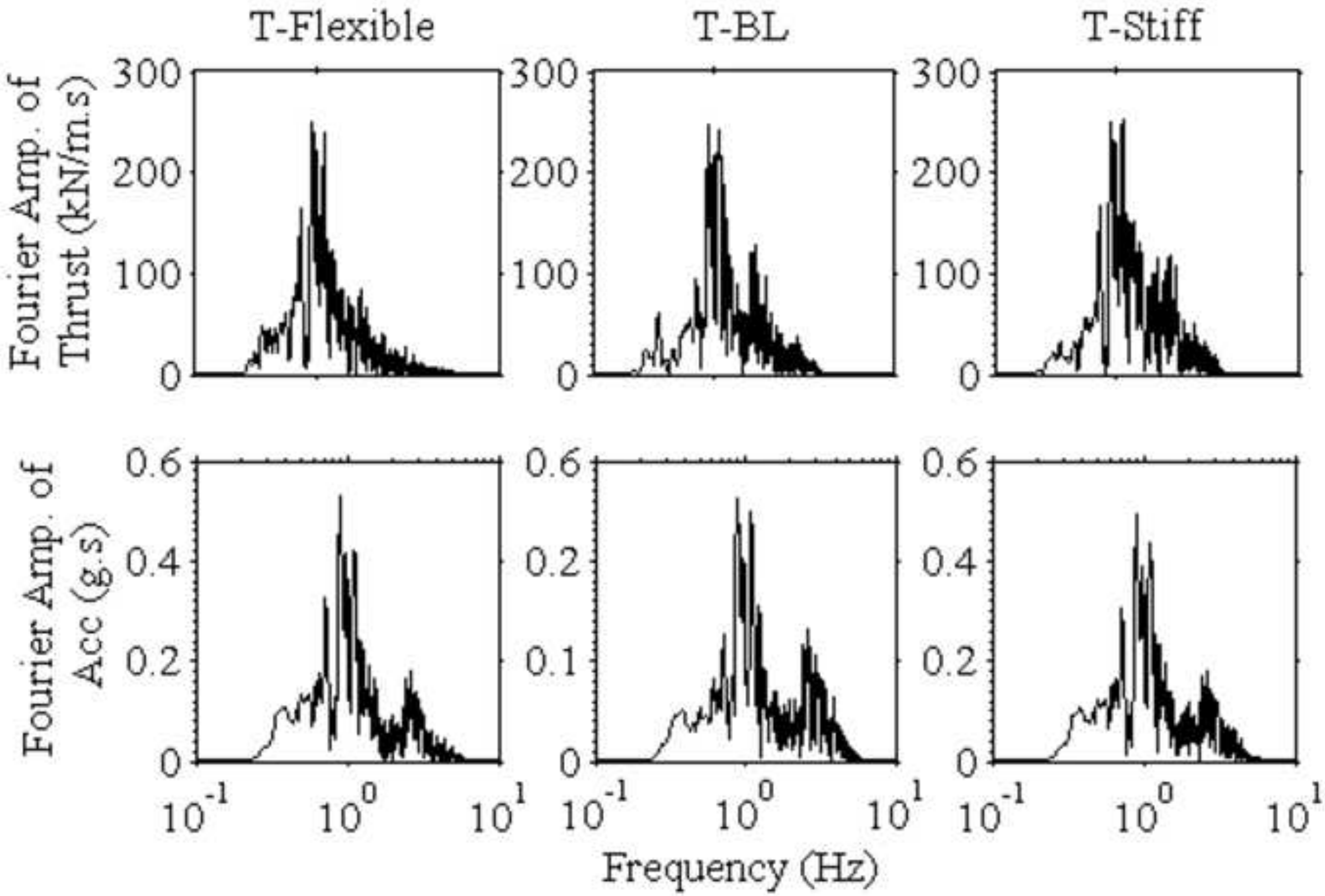
T-Flexible
T-BL
T-Stiff
Fourier Amp. of Thrust (kN/m.s)
300
200
100
0
Fourier Amp. of Acc (g.s)
0.6
0.4
0.2
0
0.6
0.2
0.1
0
10^-1
10^0
10^1
Frequency (Hz)

Figure

Click here to download Figure Figure 13.tif

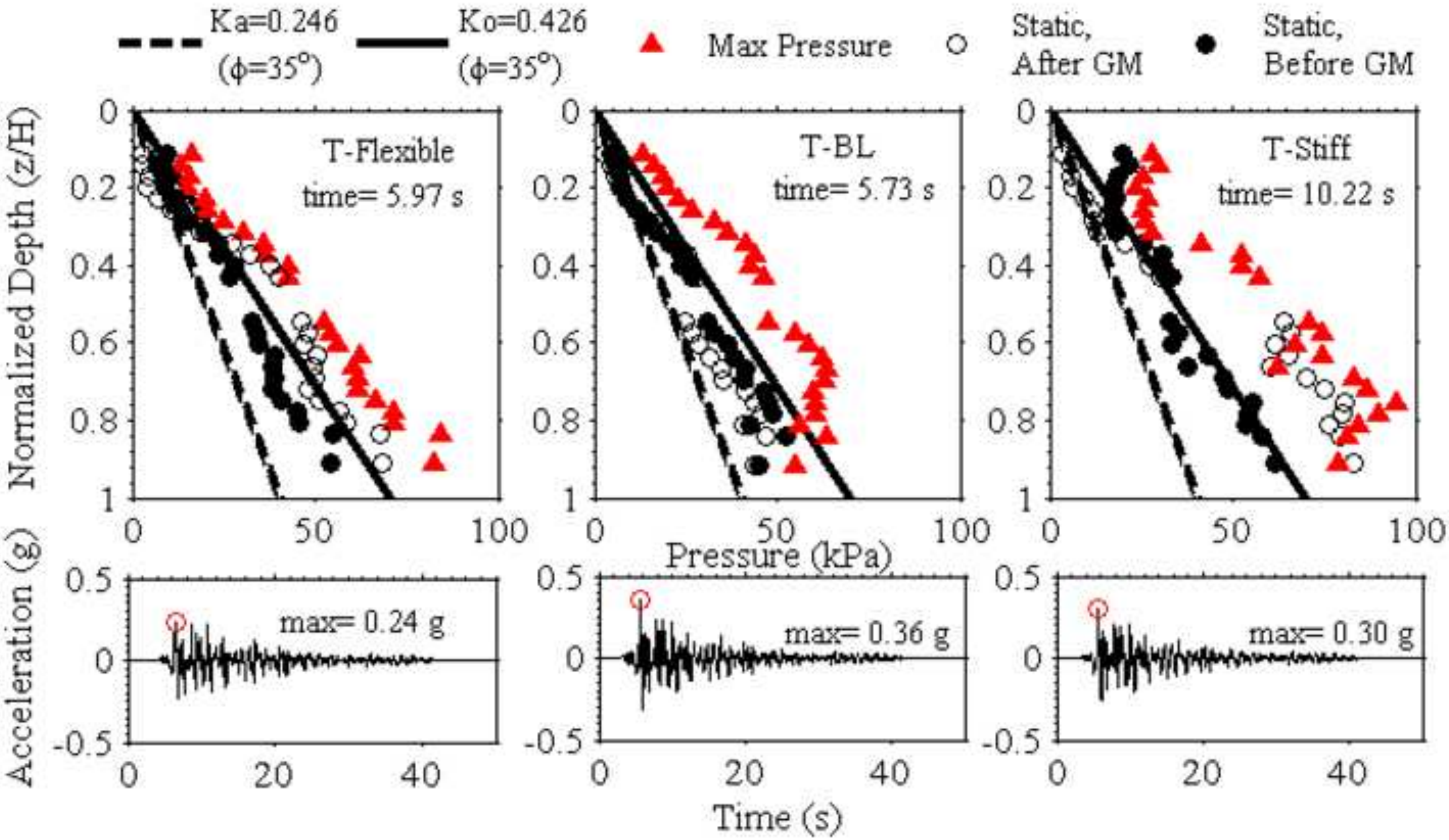

Figure

Click here to download Figure Figure 14.tif

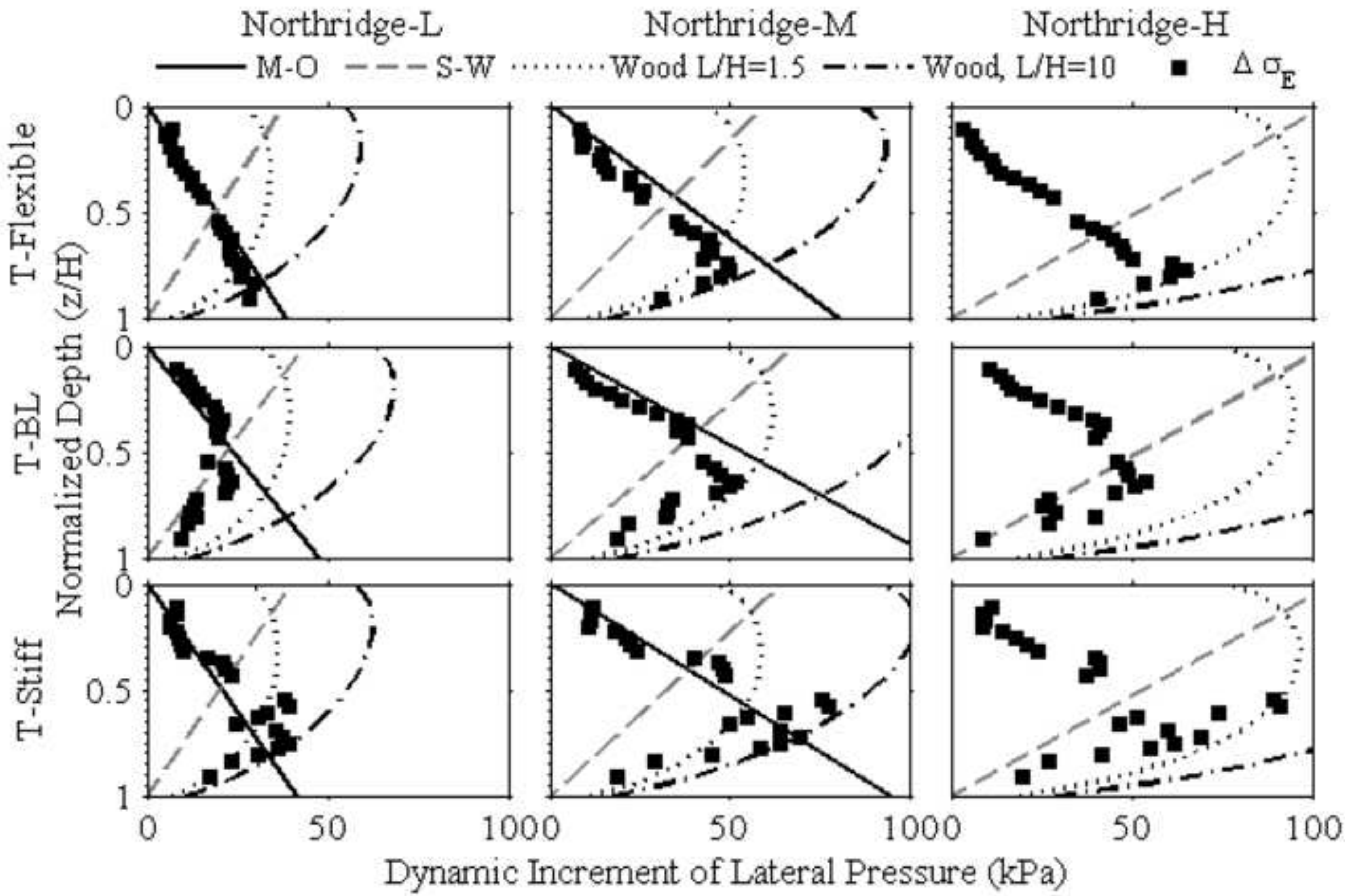

Figure

Click here to download Figure Figure 15.tif

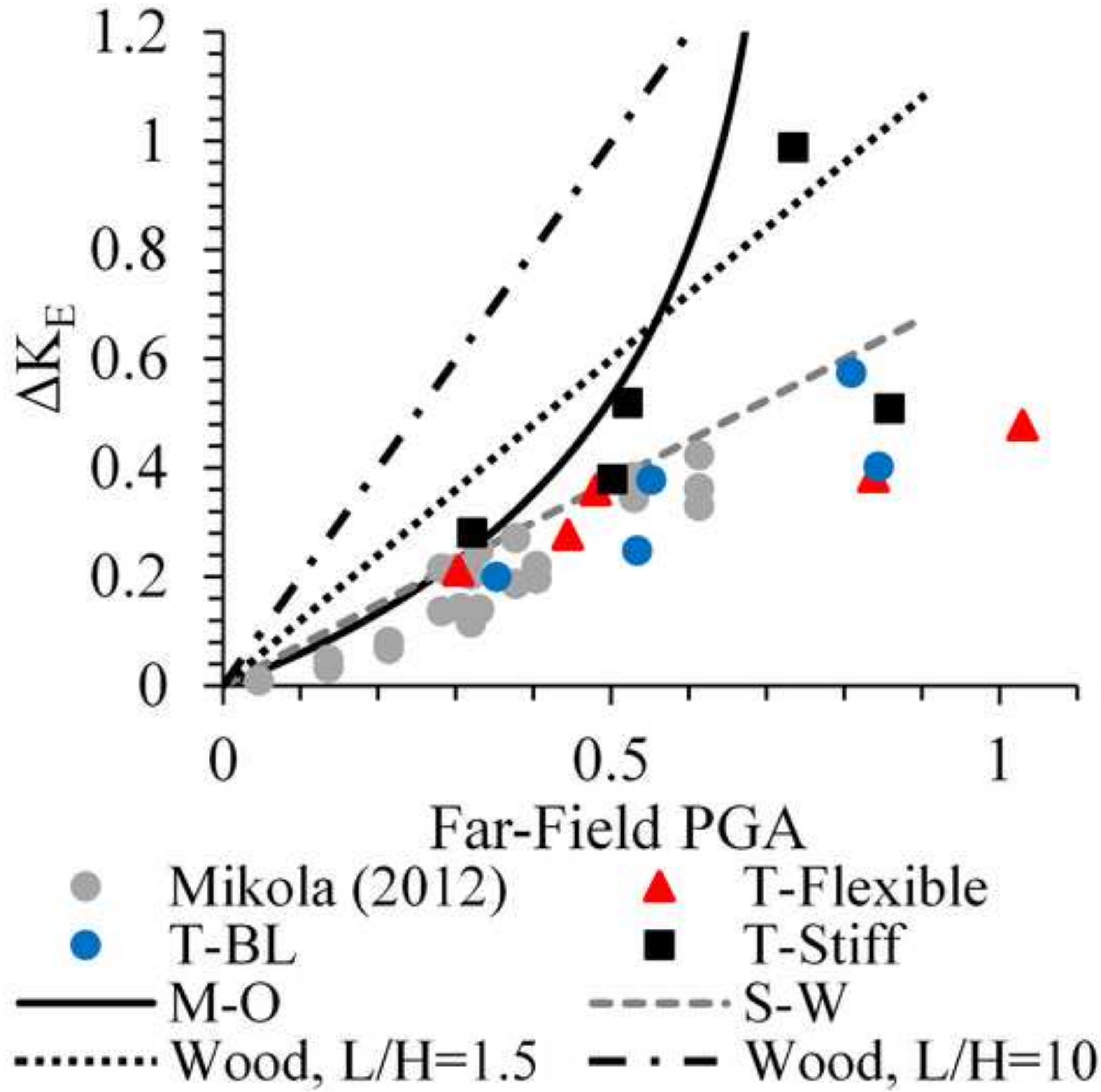

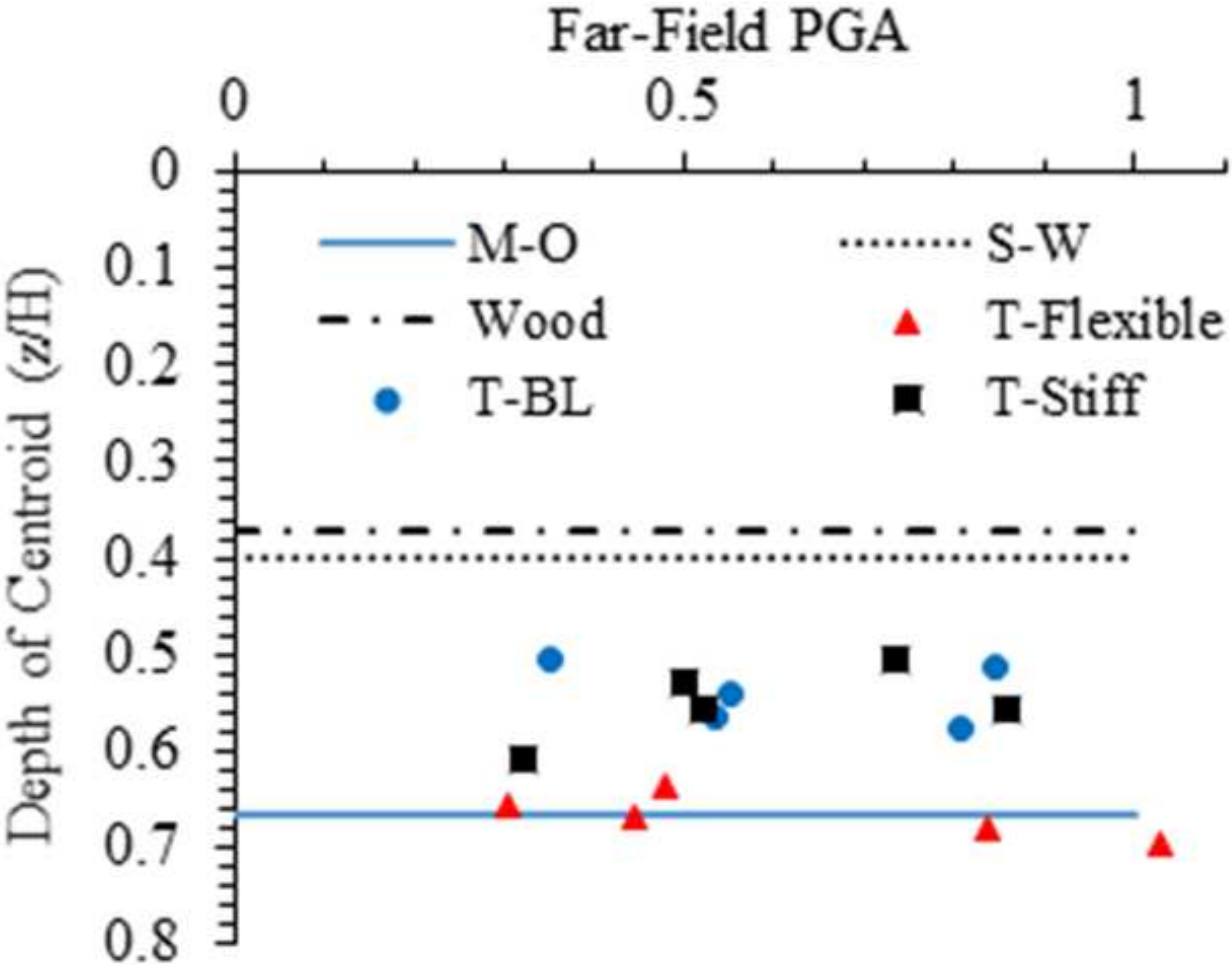
Far-Field PGA
0
0.5
1
0
0.1
0.2
0.3
0.4
0.5
0.6
0.7
0.8
Depth of Centroid (z/H)
M-O
S-W
Wood
T-Flexible
T-BL
T-Stiff

Figure

Click here to download Figure Figure 17.tif

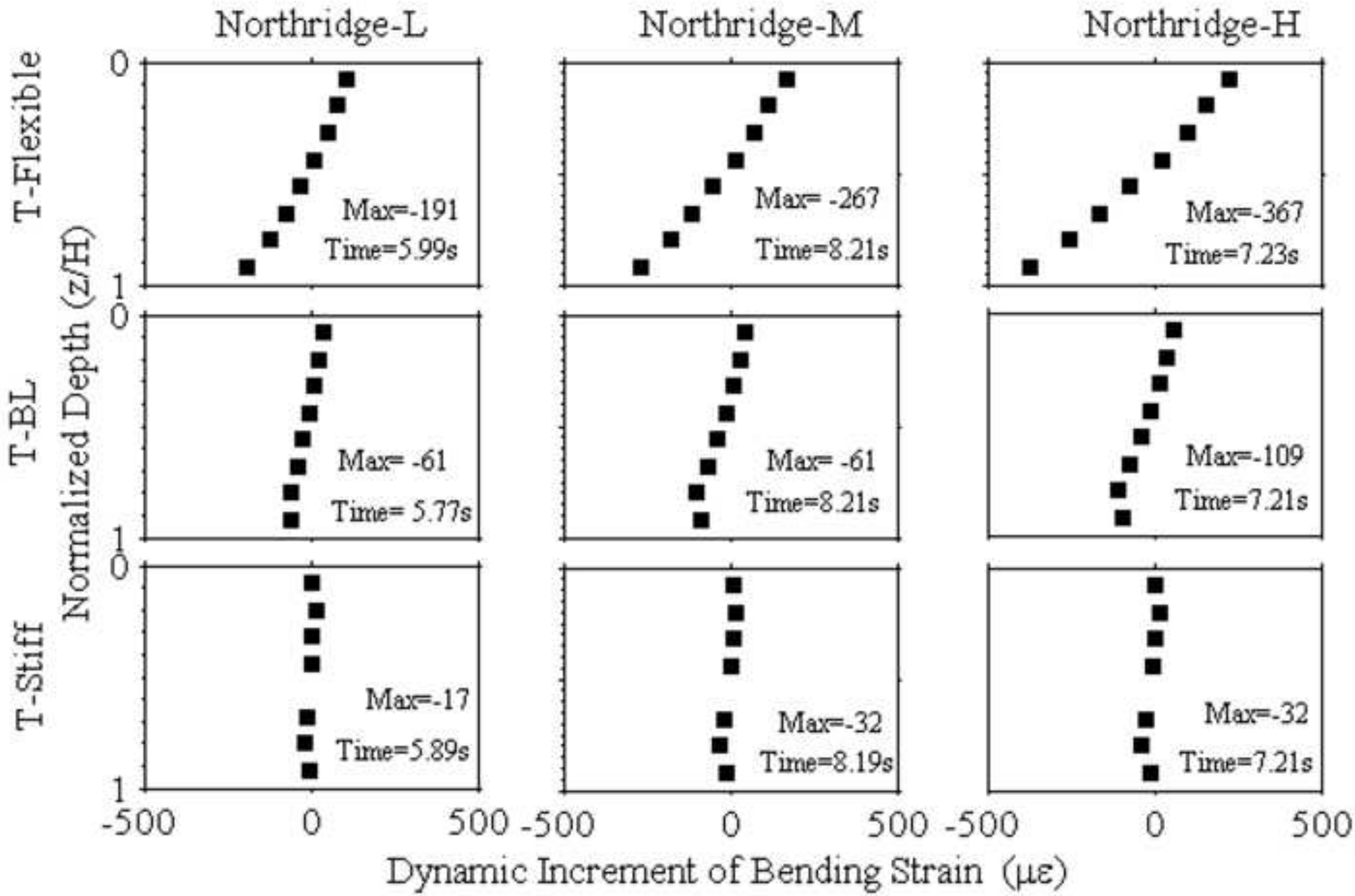

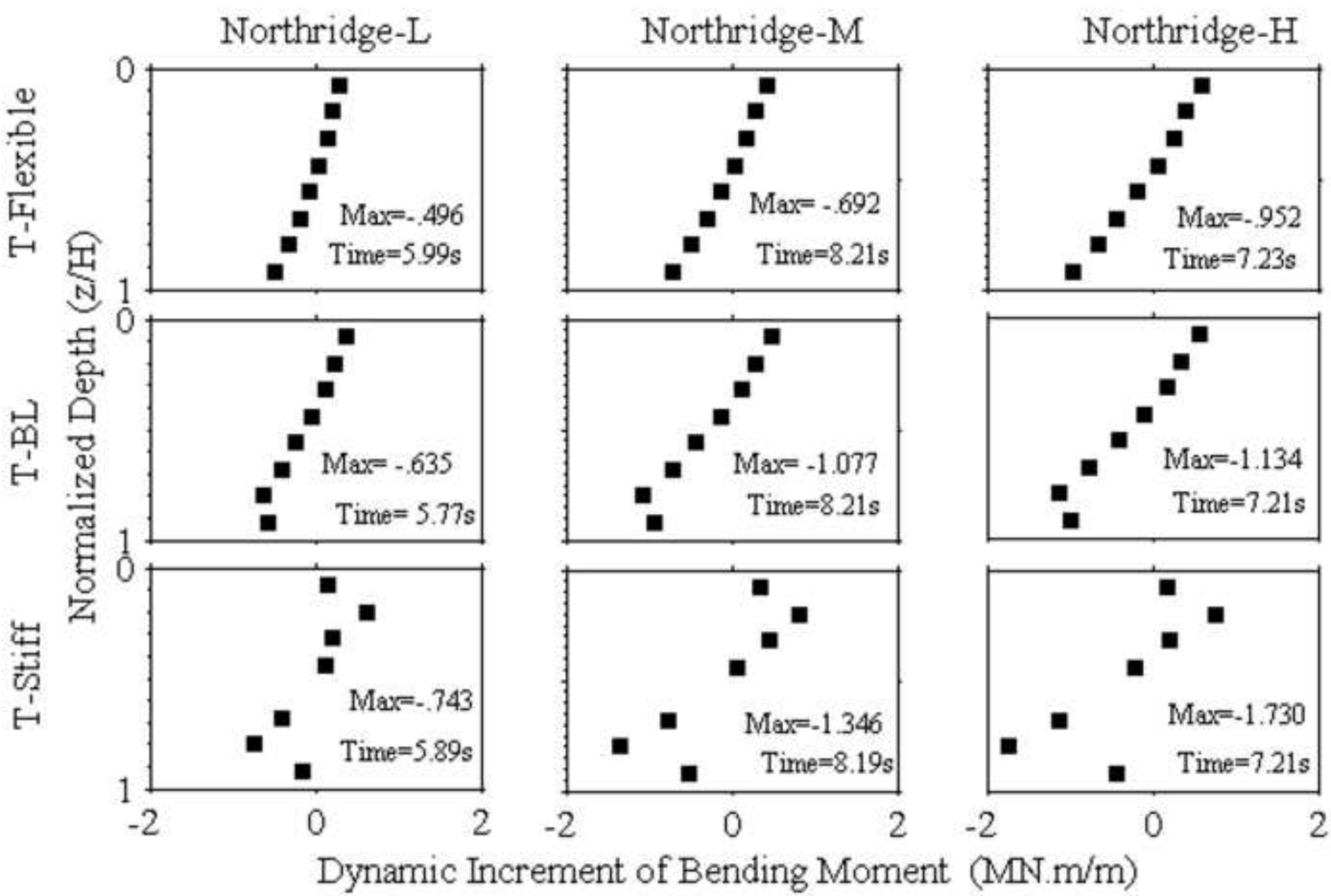

Northridge-L
Northridge-M
Northridge-H
T-Flexible
T-BL
T-Stiff
Normalized Depth (z/H)
Max=-.496
Time=5.99s
Max= -.692
Time=8.21s
Max=-.952
Time=7.23s
Max= -.635
Time= 5.77s
Max= -1.077
Time=8.21s
Max=-1.134
Time=7.21s
Max=-.743
Time=5.89s
Max=-1.346
Time=8.19s
Max=-1.730
Time=7.21s
0
1
-2
2
Dynamic Increment of Bending Moment (MN.m/m)